Universidade de Aveiro
2021

Pedro Oliveira Santos

Estudo da Resistência Mecânica de Implantes Craniais

Mechanical Strength Study of Cranial Implants

Universidade de Aveiro
2021

Pedro Oliveira Santos

Estudo da Resistência Mecânica de Implantes Craniais

Mechanical Strength Study of Cranial Implants

Dissertação apresentada à Universidade de Aveiro para cumprimento dos requisitos necessários à obtenção do grau de Mestre em Engenharia Mecânica, realizada sob orientação científica de Ricardo José Alves de Sousa, Professor Auxiliar com Agregação do Departamento de Engenharia Mecânica da Universidade de Aveiro e de Fábio António Oliveira Fernandes, Investigador Auxiliar em Regime Laboral do Departamento de Engenharia Mecânica da Universidade de Aveiro.

Esta dissertação teve o apoio dos projetos UIDB/00481/2020 e UIDP/00481/2020 - Fundação para a Ciência e a Tecnologia; e CENTRO-01-0145 FEDER-022083 - Programa Operacional Regional do Centro (Centro2020), através do Portugal 2020 e do Fundo Europeu de Desenvolvimento Regional.

o júri / the jury

presidente	**Prof. Doutor António Manuel de Amaral Monteiro Ramos** Professor Auxiliar da *Universidade de Aveiro*
vogal - arguente principal	**Prof. Doutor Marco Paulo Lages Parente** Professor Auxiliar da *Faculdade de Engenharia da Universidade do Porto*
vogal - co-orientador	**Doutor Fábio António Oliveira Fernandes** Investigador Auxiliar em Regime Laboral da *Universidade de Aveiro*

agradecimentos / acknowledgements

O primeiro agradecimento é direcionado ao Professor Doutor Ricardo José Alves de Sousa e ao Doutor Fábio António Oliveira Fernandes pela orientação prestada no decurso do trabalho, orientação essa que se veio a revelar indispensável essencialmente pela partilha e discussão de ideias. Gostaria de estender o agradecimento a todos os professores e colegas que fizeram parte deste percurso formativo, pois todos se revelaram essenciais no processo de adquirir conhecimento, culminado neste trabalho.
Um agradecimento especial à minha família e amigos próximos, pela motivação que sempre me deram.
A todos, o meu muito obrigado!

keywords Cranial Implants, Finite element method, PEEK, Cranioplasty

abstract

The human head is sometimes subjected to impact loads which lead to the skull fracture or other injuries that require the removal of part of the skull - craniectomy. Consequently, the removed portion is then replaced using autologous bone or alloplastic material. This work focuses on developing a cranial implant to fulfill the defect created on the skull and then study its mechanical performance, integrating it on the human head numerical model YEAHM. The material chosen for the implant was PEEK, a thermoplastic polymer that has been recently in use in cranioplasty. So, a numerical model head coupled with an implant was subjected to analysis to evaluate two parameters: the number of fixation screws that enhance the performance and ensure the structural integrity of the implant and the implant capacity to protect the brain compared to the integral skull. Finally, the results show that, among all tested configurations of screws, the model with eight screws presents a better performance when considering the von Mises stress field and the displacement field on the interface between the implant and the skull. Additionally, under the specific analyzed conditions, it is observable that the model with implant offers more efficient brain protection when compared with the model with the integral skull.

palavras-chave Implantes Craniais, Método dos Elementos Finitos, PEEK, Cranioplastia

resumo

A cabeça humana está, por vezes, sujeita a impactos que provocam a fratura do crânio ou outro tipo de lesões que implicam a remoção de parte do crânio - craniectomia. Consequentemente, a parte removida é posteriormente substituída usando osso autólogo ou material aloplástico. Este trabalho tem como foco o desenvolvimento de um implante cranial para preencher um defeito criado no crânio e estudar a sua performance mecânica integrando-o no modelo numérico da cabeça humana YEAHM. O material escolhido para o implante foi o PEEK, um polímero termoplástico recentemente em uso na cranioplastia. Assim, um modelo numérico Cabeça + Implante foi submetido para análise de modo a avaliar dois critérios: o número de parafusos de fixação que melhora o desempenho e assegura integridade estrutural do implante e a capacidade do implante na proteção do cérebro quando comparado com o crânio na íntegra. Finalmente, os resultados mostram que o implante, de entre todas as configurações de parafusos testadas, apresenta um melhor desempenho com oito parafusos quando analisados o campo de tensões e de deslocamentos nas zonas da interface entre o impante e o crânio. Adicionalmente, é também observável nos resultados que o modelo com implante apresenta uma eficácia de proteção do cérebro superior ao modelo com o crânio na íntegra.

Contents

List of Tables

List of Figures

List of Abbreviations

AM	Addictive Manufacture
BV	Bridging Veins
CAD	Computer-aided Design
CaP	Calcium Phosphate
CSF	Cerebrospinal Fluid
CT	Computed Tomography
EBM	Electron Beam Melting
FEA	Finit Element Analysis
FEHM	Finit Element Head Model
FEM	Finit Element Method
FFF	Fused Filament Fabrication
JC	Johnson and Cook
MRI	Magnetic Resonance Imaging
PEEK	Poly-ether-ether ketone
PEKK	Poly-ether-ketone ketone
PMMA	Poly(methyl methacrylate)
SLM	Selective Laser Melting
SLS	Selective Laser Sintering
SSS	Superior Sagittal Sinus

TBI Traumatic Brain Injury

TM Titanium Mesh

YEAHM YEt Another Head Model

Chapter 1

Introduction

1.1 Contextualisation

Cranioplasty is a medical-surgical procedure that aims to fill skull defects provoked by a craniectomy or skull fracture, recovering its protective function and also bringing back aesthetic satisfaction to the patients.

Craniectomy is an emergency surgical procedure where a part of the patient's skull is removed to reduce the pressure on the brain, resultant from swelling or bleeding. Then, when the brain's pressure decreases, the surgeon fills the gap in the skull using autologous bone or alloplastic materials.

Nowadays, the evolution occurred in Computer-Aided Design and Addictive Manufacture guided to an increase of patient specific cranial implants production in cranioplasty. These implants have multiple advantages, among which are included a good definition on the implant contour and high precision on curvature, both adapted to the patient's necessities. Also, it reduces the risk of surgical complications and increases the aesthetic results [Huys *et al.* 2021].

In order to test the protective capacity of the skull, the fact that the patients need to return to their normal life requires knowledge about implants' capacity to resist to impact loads. So, numerical simulations are powerful tools that allow to measure mechanical strength, identify critical regions on the implant and predict brain injuries without having to subject the materials to mechanical testing [Huys *et al.* 2021]. Therefore, numerical simulations, such as finite element analysis, act as a tool to spare animals or humans from the testing and to prevent material waste [Barbosa *et al.* 2020].

All the parts of the human head and their mechanical properties are crucial to protect the brain against impact loads. So, to be able to perform the numerical simulations on a finite element head model developed in detail constitutes a great step up on this area.

1.2 Goals and Contributions

The main purposes of this work are to study the mechanical resistance of a cranial implant and find a solution that reaches a good integration on the skullbone, an effective mechanical performance and aesthetical results that match an integral human skull. Also, the design of a cranial implant which can be obtained by addictive manufacture is also a big ambition.

1.3 Reading Guide

This work is divided in six main parts, and this section offers a brief description of what each of them contains.

- Chapter 1 - Introduction

  This chapter contains all the introductory information about the work and its topics, the motivations and goals and the structure;

- Chapter 2 - State of the Art

  After an intensive literature review, this chapter contains the most relevant information about the topics discussed in this work and intends to give the reader tools to better understand all the decisions and argumentation made further in the work;

- Chapter 3 - Implant Material

  This chapter presents a description of the constitutive material model chosen for the implant and the arguments that lead to its choice;

- Chapter 4 - Methodology

  Having enough information about the topics, this chapter contains information about the steps for the skull's defect creation, implant's geometry and mesh creation and modeling strategies;

- Chapter 5 - Numerical Simulations and Results

  As the name implies, this chapter contains a brief preamble about the conditions of the simulations and presents the results and respective reading;

- Chapter 6 - Conclusion

  Finally, this chapter include the final considerations about the work, as well as suggestions for future works.

Chapter 2

State of the Art

2.1 Human Head Anatomy

2.1.1 Skull

The human skull is an extremely important part of the human body mainly because it has the task of protecting the brain, which is the most important organ of the human body. It is possible to divide the skull into two parts: the braincase (neurocranium) and and the facial skeleton (viscerocranium). In terms of bones, the cranial part contains the occipital, two temporal, two parietal, sphenoid, ethmoid and frontal, while the facial part contains the vomer, two nasal conchae, two nasal bones, two maxillae, mandible, two palatine, two zygomatic, two lacrimal (Figure 2.1) [Becker 2021].

Cortical Bone and Trabecular Bone

The human skeleton is composed of both cortical bone and trabecular bone. Cortical bone is treated as a compact bone taht act as the outer layer of the skeleton, surrounding the trabecular bone and providing a hard covering for the skeleton. Also, it is composed of microscopic units, the haversian systems [Evans 2012].

On the other hand, trabecular bone is a spongy-like tissue configured in a lattice consistency situated in the core of bones. Figure 2.2 contains a representation of both bone types and its architecture.

Cranial Sutures

Cranial sutures act as a connector of the skull's bones and are composed mainly of collagen. There are three cranial sutures: coronal, sagittal and lambdoid (Fig. 2.3) [Ptak *et al.* 2018]. The mechanical properties of cranial sutures is a sensitive issue and do not gather consensus, which is related to the different distribution of collagen fibers, causing different mechanical properties and geometries [Ptak *et al.* 2018].

2.1.2 Brain

Treated as one of the largest and most complex human organs, the brain is responsible for multiple tasks, such as translating sensations, thinking, coordinating movements, controlling sleep and breathing patterns [Plutchik and Kellerman 1986]. Alongside the

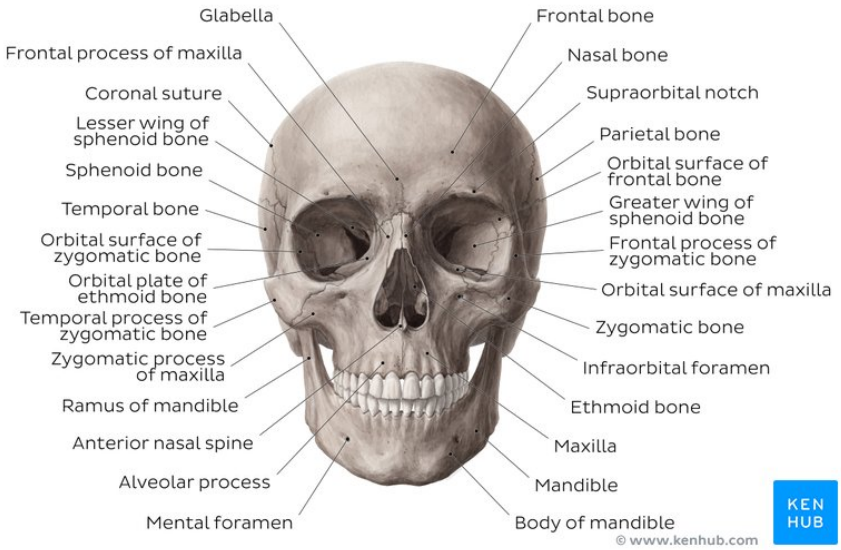

Figure 2.1: Skull anterior view [Becker 2021].

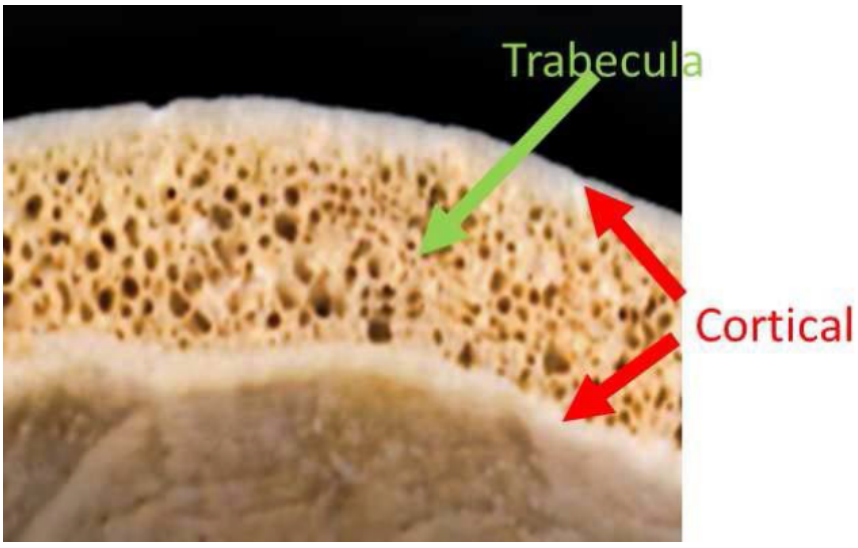

Figure 2.2: Cortical and trabecular bone layers in skull [Wang *et al.* 2014].

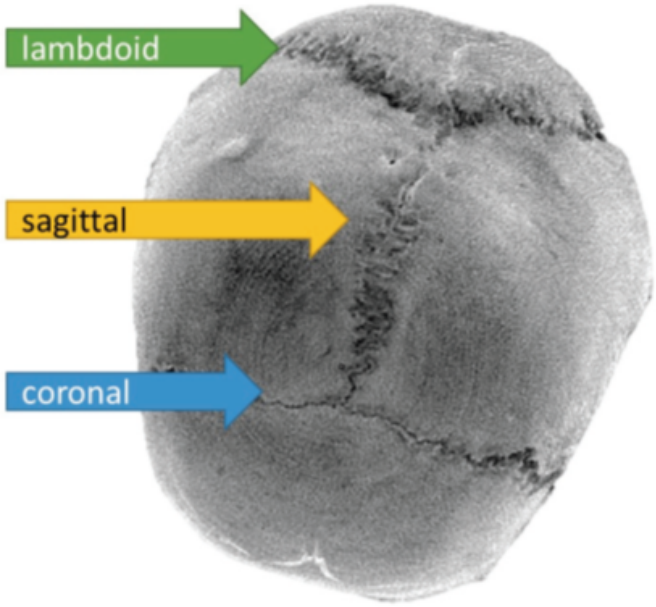

Figure 2.3: Cranial sutures [Ptak *et al.* 2018].

spinal cord, is the main organ of the central nervous system and can be divided into three different parts: cerebrum, cerebellum and brainstem [Shahid 2021]. The cerebrum, largest part of the brain and situated in cortex (Fig. 2.5), consists of four paired lobes (frontal, parietal, temporal and occipital), represented in Figure 2.4, the brainstem connects all the brain's parts and the cerebellum is responsible for the smoothness of our movements [Shahid 2021]. Also, the brain is situated in the neurocranium and involved by the cerebrospinal fluid (CSF).

Since the brain is a very sensitive organ and needs the protection of all parts that surround it against impact loads, a good indicator of the effectiveness of external parts, like a cranial implant, is the capacity to protect the brain against severe injuries. So, Tse et al. [Tse *et al.* 2015] compiled a set of criteria related to mechanical variables like pressure, shear stress, von Mises stress and strain that allows measuring traumatic brain injury (TBI) [Garcia-Gonzalez *et al.* 2017]. TBI can be classified as a combination of two parameters: deformation processes due to brain motion and indentation process on the skull (or implant) [Garcia-Gonzalez *et al.* 2017]. Table 2.1 contains the thresholds of brain injury criteria.

2.1.3 Meninges

The meninges are defined as the three layers covering all the components of the central nervous system. The pia mater is the closest one from the structures, being closely attached to them. On the other hand, the arachnoid mater is right upon the pia mater, and between these two layers is the space where the blood vessels that supply the brain are situated. Finally, the dura mater is the most distant layer from the structures, contacting with the internal surface of the skull [Shahid 2021]. The multiple layers of the meninges are represented in Figure 2.6.

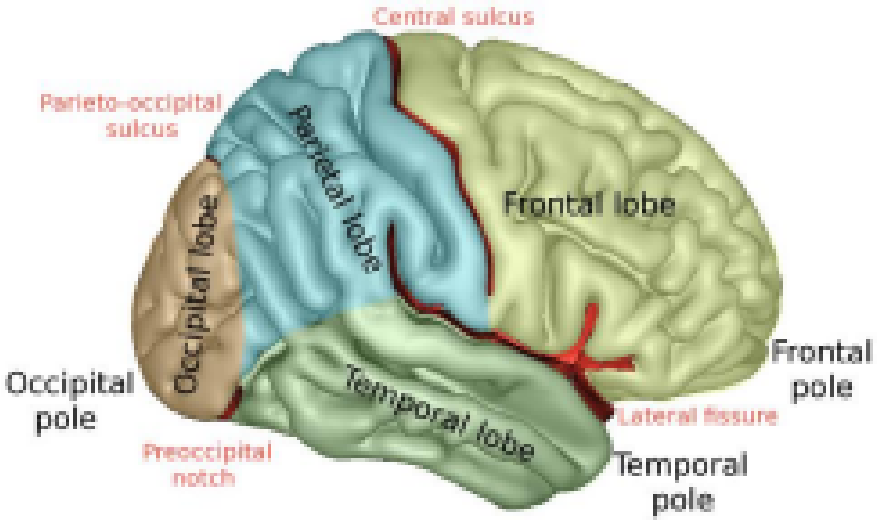

Figure 2.4: Lateral view of right cerebral hemisphere with main lobes [Nocerino *et al.* 2017].

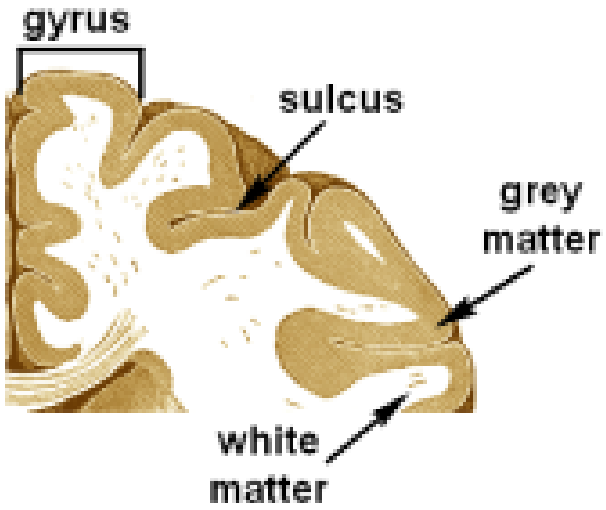

Figure 2.5: Cortex structure of brain [Nocerino *et al.* 2017].

Table 2.1: Thresholds of brain injury criteria [Tse *et al.* 2015].

Parameter	**Thresholds**
Pressure	***Criterion 1***
	>235 kPa → injury
	<173 kPa → minor or no injury
Shear stress	***Criterion 2***
	11–16.5 kPa → severe injury
von Mises stress	***Criterion 3***
	>18 kPa → 50% probability of moderate neurological lesions
	>38 kPa → 50% probability of severe neurological lesions
	Criterion 4
	≥ 26 kPa → axonal damage
Strain	***Criterion 5***
	>0.25 → structural damage
	>0.20 → functional damage
	>0.10 → reversible damage

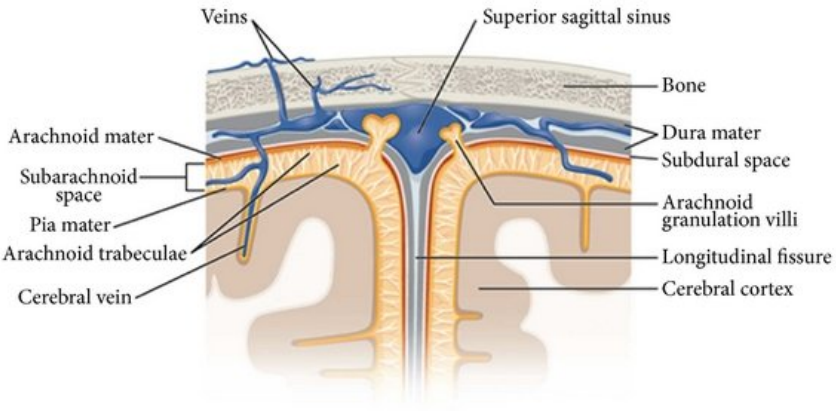

Figure 2.6: Layers that make up meninges [Saboori and Sadegh 2015].

2.1.4 Cerebrospinal Fluid

Cerebrospinal Fluid (CFS) is a plasma-like fluid that involves the structures of the central nervous system. CSF flows between cavities situated in the brain and spinal cord such as ventricles, subarachnoid space of the brain and spinal cord and the central canal of the spinal cord (Fig. 2.7). Also, CSF aggregates a lot of important functions: dampen the brain and spinal cord when they are subjected to external forces, transport neuromodulators and neurotransmitters, give immunological protection and remove metabolic waste [Sendic 2021].

From the point of view of this work, the most important function of the CSF is the mechanical protection that it provides against shocks, acting as a shock absorber, which is crucial to prevent brain injuries [Sendic 2021].

2.1.5 Bridging Veins

The main function of bridging veins (BV) is to drain the venous blood from the cerebral cortex into the superior sagittal sinus (SSS), bridging the subdural space, i. e., the space between the dura mater and arachnoid mater. Their mechanical properties are not very well known even though they are very important in head impact biomechanics [Famaey *et al.* 2015]. Figure 2.8 (a) and 2.8 (b) contains a detailed view over the bridging veins and its assembly in the head structures, respectively.

The cranial end of the bridging veins is fixed to the dura mater while the cerebral end is fixed to the hemispheres. Since there is no protection against antero-posterior movement of the brain, an impact on the head resulting in this type of movement can provoke the rupture of the bridging veins [Famaey *et al.* 2015].

The direction of flow from the bridging veins into the SSS is very variable and this can cause relative movements between brain and skull, which results in tensile and shear loadings causing some lesions [Famaey *et al.* 2015].

2.2 Materials For Cranioplasty

2.2.1 Autograft and Allograft

Autograft therapy (Fig. 2.9) is commonly used in all human body parts and is the most ancestral surgical therapy when referring to cranial defects. Yet, there are some limitations: the supply of graft material is limited by donor site size; autograft harvesting risks long-term donor site pain; and the grafted bone may fail to vascularize [Bonda *et al.* 2016]. Thus, this strategy is time-consuming, cumbersome and may lead to long-term infections and pain at the donor site [Bonda *et al.* 2016].

On the other hand, allograft therapy, by cadaver or live bone donation, is a tough strategy due to the risk of immunological rejection and pathogen transmission. Unlike autografts, there is no problem associated with donor site morbidity, nevertheless, there is an increase in the risk of disease transmission and infection [Bonda *et al.* 2016].

2.2.2 Metal Bone Substitutes

The use of metal as a bone substitute is, undoubtedly, a conventional technique. The most usual metal is grade 5 surgical titanium (Ti-6Al-4V), which is used in the cranium

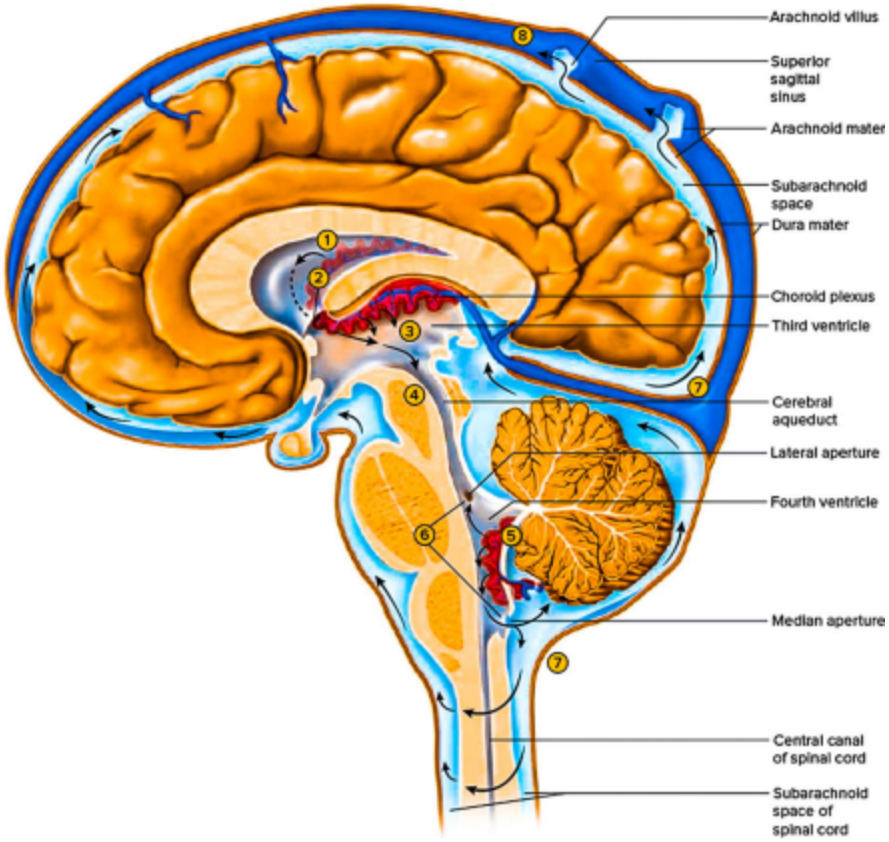

Figure 2.7: Cerebrospinal fluid (CSF) formation, absorption and circulation around the brain [Donatelli and Romagnoli 2020].

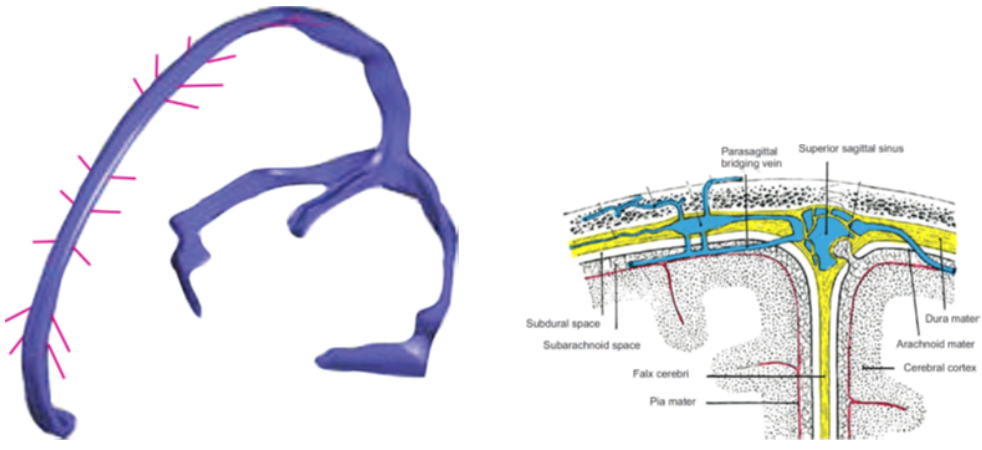

(a) (b)

Figure 2.8: (a) Detailed view over the bridging veins and (b) frontal view over the head containing the bridging veins, skull, meninges and brain [Famaey *et al.* 2015].

Figure 2.9: Autograft in cranioplasty [Zhang *et al.* 2019].

for fixation devices or in combination with other materials like inert plastic or ceramic components [Bonda *et al.* 2016]. Despite the fact that titanium is corrosion-resistant, there is evidence that trace minerals are released over time, which may lead to an immunologic response [Bonda *et al.* 2016]. Also, some problems related to the interaction with the overlying scalp flap and underlying alloplastic materials can cause inflammation, infection, or implant fenestration through the scalp. These materials are also known for being incompatible with computed tomography (CT) and magnetic resonance imaging (MRI), very important techniques to monitoring bone growth and healing [Ma *et al.* 2021].

When talking about the mechanical properties, it is extremely important to make a comparison between the titanium and the skull. Ti-6Al-4V elastic modulus assumes values of 14,5-38,5 GPa for porous implants, like the one represented in Figure 2.10, and 110 GPa for bulk specimens. Moreover, the skull elastic modulus is located between 10,4-19,6 GPa. As a consequence, the titanium implants may break the surrounding bone or suffer a fixation screw pull-out [Bonda *et al.* 2016].

2.2.3 Polymers Bone Substitutes

Poly(methyl methacrylate) (PMMA), represented in Figure 2.11, as a huge role in cranioplasty simply because it is the most used cranial bone graft substitute and one of the earliest [Bonda *et al.* 2016, Zhang *et al.* 2019]. PMMA has a lot of advantages by being a protective, defect-filling replacement that lacks post-operative inflammation [Bonda *et al.* 2016]. Nonetheless, the polymerization process is exothermic and the heat generation may damage the surrounding brain tissue. Also, there is the possibility of post-placement shrinkage, infection and pulmonary embolism [Bonda *et al.* 2016]. Maybe the major disadvantage associated with PMMA is the fact that it lacks the osseointegrative and osteoinductive properties that would provide complete regeneration of reliable bone [Bonda *et al.* 2016]. However, PMMA mechanical properties are much similar when compared with the skull. The elastic modulus is approximately 3 GPa which may lead to a lesser discontinuity at the implant-skull interface (mainly when

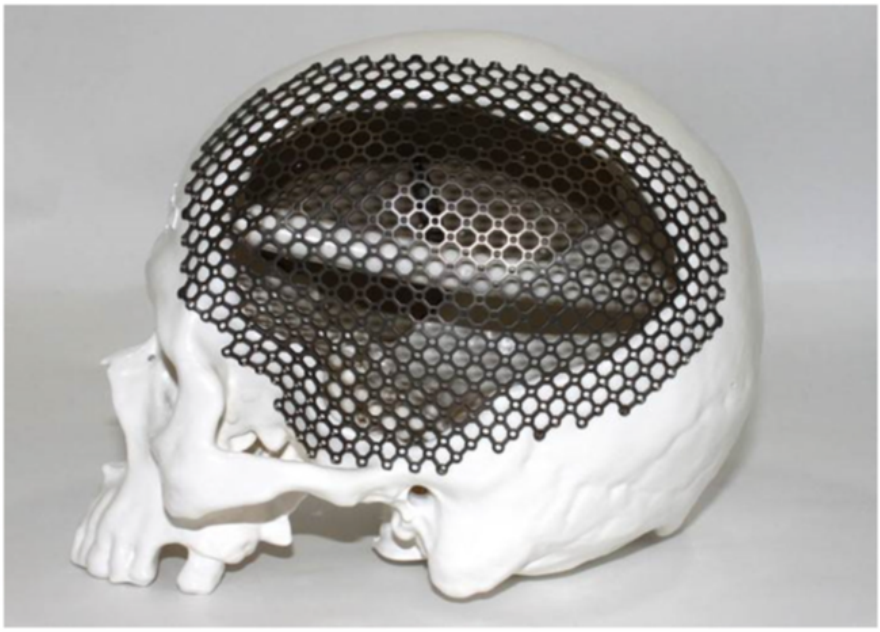

Figure 2.10: Titanium mesh cranial implant [Bonda *et al.* 2016].

compared to titanium) [Bonda *et al.* 2016].

Some other polymers have been in use and the investigation on this subject are going on. Polyethylene, which has the risk of infection, has also been in use, with PEEK (poly-ether-ether ketone) and PEKK (Poly-ether-ketone ketone) emerging with a lot of potential as their mechanical properties are very similar to the surrounding bone [Bonda *et al.* 2016].

2.2.4 Ceramic Bone Substitutes

Calcium phosphate (CaP) is a controversial bone substitute, frequently treated as a tissue engineering scaffold. This shapable material is extremely brittle and is commonly used to fill minor gaps in the skull [Bonda *et al.* 2016].

2.2.5 PEEK As An Emerging Material

In order to understand why PEEK is being so much employed in cranioplasty, it's important to review some problems related to the use of traditional materials. Stainless steel and titanium alloy have high mechanical strength, excellent bio-compatibility and good fatigue resistance. Yet, these materials' elastic modulus is much higher than bone tissue. As a consequence, the stress stimulation value of the bone in the areas around the implant is lower than the value required to promote bone regeneration. Thus, the bone around the implant is absorbed and its strength reduced, leading to the "stress shielding" phenomenon [Ma *et al.* 2021].

PEEK is a polyaromatic semi-crystalline thermoplastic polymer (with its chemical formula represented in Figure 2.13) used in spine surgery, orthopedic surgery, prosthodontics surgery, maxillo-facial surgery and cardiac surgery and, more recently, cranioplasty (Fig 2.12). This new type of thermoplastic has excellent biological, mechanical and

Figure 2.11: PMMA cranial implant [Bonda *et al.* 2016].

chemical properties. Its biomechanical properties (elastic modulus about 2–6 GPa) are close to human bones, which can reduce the risk of bone resorption and the effect of stress shielding (a problem associated with metallic implants). Also, there are a lot of advantages like the high thermal stability, toughness and rigidity, the facility to process, self-lubrication and abrasion resistance [Ma *et al.* 2021].

When comparing PEEK implants with autologous bone, the rapid conclusion is that PEEK implants are superior in aspects such as treatment success, complication rate, hospital stay and operation time. In fact, many problems related to autologous bone, like bone reabsorption, infection and donor-site morbidity, can be solved by using PEEK implants, despite their higher cost, harder patient incorporation and less cosmetic satisfaction [Zhang *et al.* 2019].

Furthermore, it has been shown that choosing PEEK over titanium mesh leads to a better cosmetic satisfaction and brain function improvement aspects, with no concrete conclusions on matters like operation time and hospital stay. Thus, titanium mesh implants are easily deformed by the same force as PEEK ones, which results in brain damage and appearance modification, leading to an eventual need for replacement [Zhang *et al.* 2019].

PEEK and PMMA implants are very identical in terms of complication rate and treatment success rate. Moreover, the fact that PMMA implants have a negative impact on the surrounding tissues and a high infection rate means PEEK implants are a more suitable option [Zhang *et al.* 2019]. Table 2.2 contains the comparison between the properties of the most common materials used in cranioplasty.

On the other hand, pure PEEK is not bioactive, so, in order to promote osseointegration with bone tissue, there are two strategies: create composite materials by adding to PEEK matrix active materials (bioactive glass, carbon fiber or HA, among others) or create a

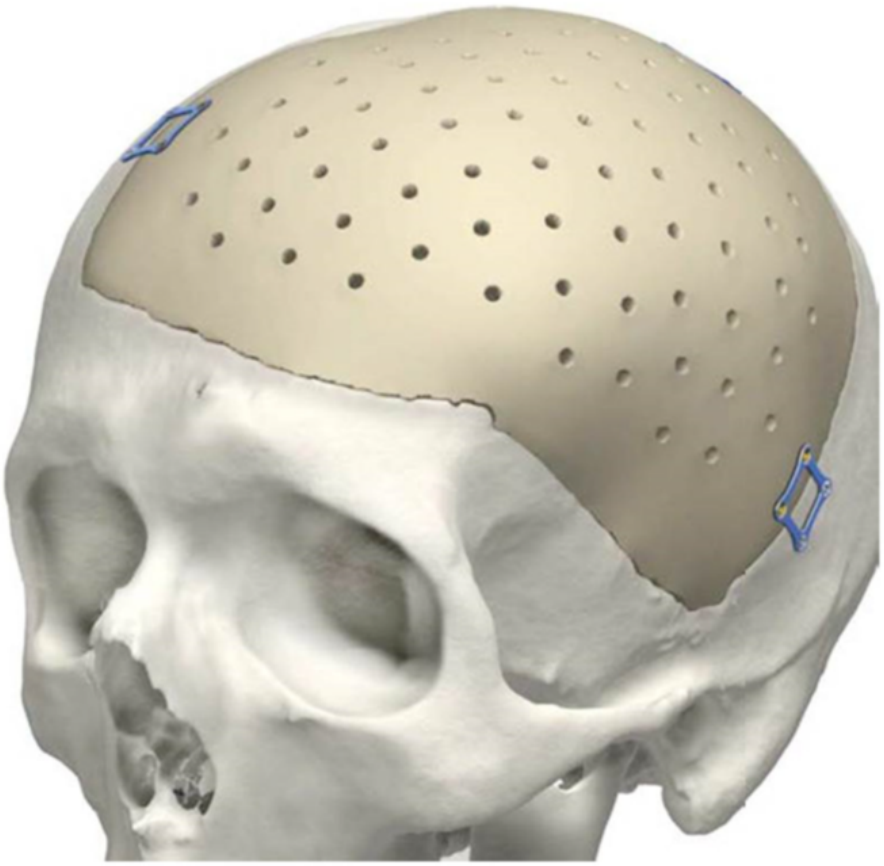

Figure 2.12: PEEK cranial implant [Bonda *et al.* 2016].

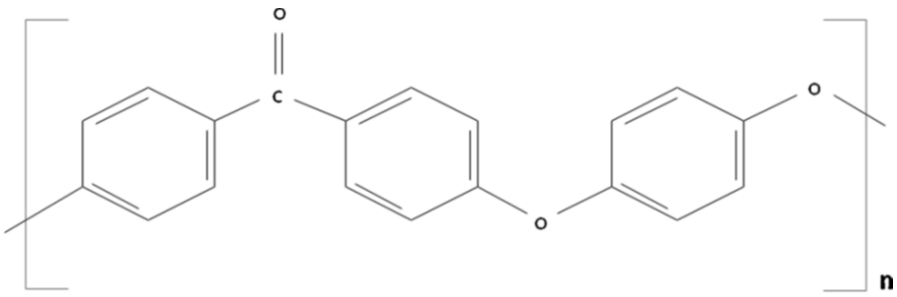

Figure 2.13: Chemical structure of monomer unit of polyetheretherketone (PEEK) [Zhang *et al.* 2019].

Table 2.2: Properties of the most common materials employed in cranioplasty [Zhang *et al.* 2019].

Materials	Tensile strength (MPa)	Young's modulus (GPa)	Fracture Resistant	Biocompatibility	Osteointegration
PEEK	80-132	3-4	Very High	High	No
Autologous bone	104-121	7-30	High	Very High	Yes
TM	954-976	102-110	High	High	No
PMMA	48-76	3-5	High	Good	No
Materials	**Toxicity**	**Radioluncency**	**Resterilization**	**Porosity**	**Cold and Heat Conductance**
PEEK	No	Yes	Yes	Yes-Very Few	No
Autologous bone	No	Yes	Yes	Yes	No
TM	Possible	No	Yes	Yes	Yes
PMMA	Possible	Yes	No	No	No
Materials	**Aesthetic Results**	**Costs**	**Infection Rate**	**Complication rate**	**Intraoperational Workable**
PEEK	Excellent	High	Moderate	Low	Yes
Autologous bone	Excellent	Low	Moderate	Low—moderate	Yes
TM	Satisfying	Moderate	Low—moderate	High	No
PMMA	Satisfying	Moderate	High	Low	Yes

scaffold.

2.3 Cranial Implants Design and Manufacture Strategies

2.3.1 Cranial Scaffolds

In simple words, scaffolds are matrices with complex noncellular structural networks (Fig. 2.15 offers an example of a network) that helps binding cells and, consequently, the tissue formation [Roque *et al.* 2021]. This matrix and its parameters are responsible for controlling the growth and formation of the tissue, which makes it an important tool for tissue engineering [Roque *et al.* 2021].

The already mentioned scaffold parameters assume a huge role in tissue formation, and, for that reason, they need to be controlled. The most important ones can be described as surface area and interconnectivity (responsible for cellular growth), permeability (related to transportation of nutrients and proliferation of tissue) and mechanical resistance (responsible for the protection capacity) [Roque *et al.* 2021].

In order to solve the problems associated with the excess of lactic acid due to normal implant degradation in patients involving large resorbable Poly(α-hydroxy ester)-based prosthetics, like PLGA or PLA, the use of scaffolds structures can be a feasible solution. This strategy can solve this issue by using 3-D printed polycaprolactone (PCL), via FFF (Fused Filament Fabrication). Thus, there are studies that show the effectiveness of the implantation of a 3-D printed PCL and tricalcium phosphate cranial scaffold, with evidence proving bone consolidation and good integration of the implant after approximately 6 months [Bonda *et al.* 2016]. Figure 2.14 offers an example of a PEEK scaffold.

2.3.2 CAD For Cranial Implants

As a crucial step for the implant design, computer-aided design for this type of component can follow some templates, like an average skull or a left-right mirrored image (in the case of a one-sided defect). Next, the template is warped to the skull defect and the part of the template that fills the defect is cropped. Moreover, thickness is added to create a

Figure 2.14: PEEK scaffold cranial implant [Berretta *et al.* 2018].

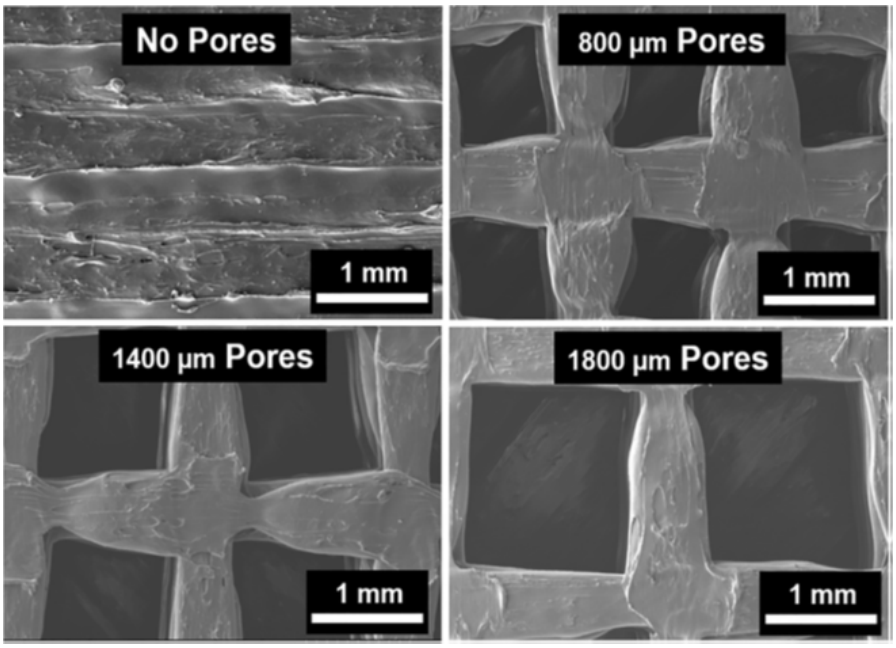

Figure 2.15: Macroporous PEEK scaffolds [Elhattab *et al.* 2020].

tapered edge that overlaps the surrounding skull [Bonda *et al.* 2016]. The steps of this process are exemplified in Figure 2.16.

When creating a PEEK implant with no porosity, there is the necessity to incorporate small holes in to help dural tack-up sutures and muscle suspension (Fig. 2.17) [Jonkergouw *et al.* 2016]. Otherwise, when incorporating tissue engineering during implant development, CAD techniques should be employed to obtain the scaffold structure during the design process (Fig. 2.18) [Huang *et al.* 2019, Elhattab *et al.* 2020, De Santis *et al.* 2021, Roque *et al.* 2021].

2.3.3 Additive Manufacture For Cranial Implants

The technologies used to fabricate cranial implants by additive manufacture depend on the material family. In the case of metal, Ti-6Al-4V can be obtained via selective laser sintering (SLS), selective laser melting (SLM) and electron beam melting (EBM). Amongst these technologies, there is the possibility to create scaffold structures [Bonda *et al.* 2016].

On the other hand, synthetic polymers for addictive manufacturing of cranial implants are the most employed technique. Since working with PMMA is a hard task, PEEK obtained via SLS has been exploited by every company in this area. As an advantage, the design of the implants can be modified to make material properties similar to the adjacent skull, making PEEK cranial implants more suitable than titanium ones when talking about this matter [Bonda *et al.* 2016].

Otherwise, ceramic is a great scaffolding material in sub-critical size defects, like mentioned previously. However, stereolithography is proving to be a good technology to obtain large ceramic cranial implants. Studies have shown the potential of 3-D printing a ceramic cranial implant using a polymer blinder which is then sintered away. Investigations are being held in order to develop a composite material composed of 50% Beta-tricalcium phosphate (B-TCP) and 50% poly(D,L)-lactide (PDLLA) that is obtained via SLM [Bonda *et al.* 2016].

2.3.4 Fixation Methods

Fixation methods in cranioplasty are frequently chosen by the surgeon, based essentially on the experience. There are a lot of fixation devices, with the most employed ones being titanium miniplates (Fig. 2.20), titanium tangential screws (Fig. 2.21) and titanium clamps (Fig. 2.22). The chosen fixation method, as well as the number of fixation points, are variables that play a huge role in avoiding the displacement of the implant.

As shown in related studies [Rashidi *et al.* 2019], the probability of occurring the displacement of the implant when the implant is fixed with titanium clamps is four times higher than when the fixation devices are miniplates, meaning that using titanium clamps as the main fixation method is a risk factor to the occurrence of implant displacement. Despite leading to higher strain in the interface between bone and implant, tangential screws offer a more rigid fixation and, since it is directed tangentially into the bone, this method is completely impalpable. These are the main reasons why it is the preferred method nowadays [Huys *et al.* 2021].

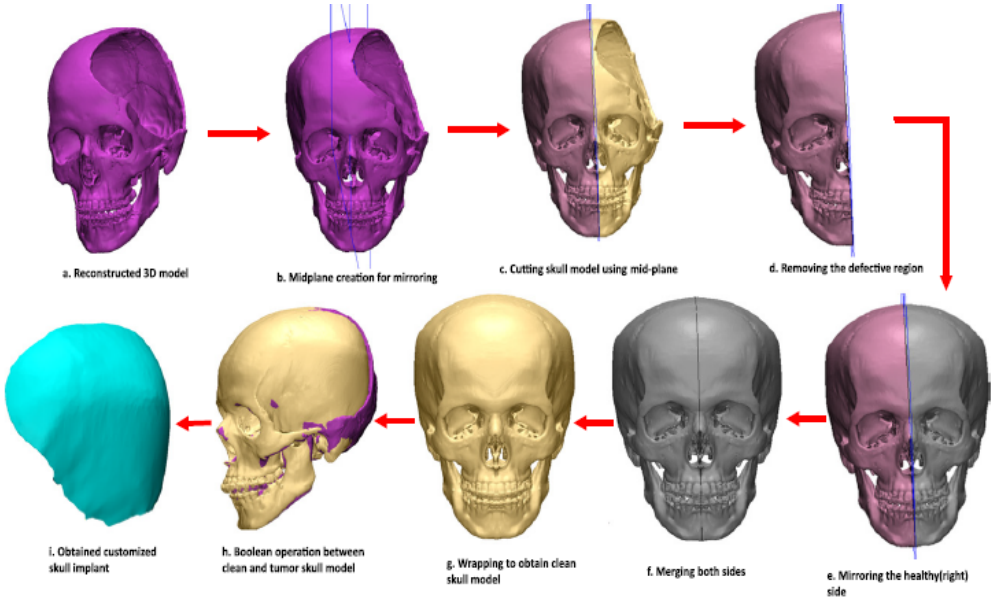

Figure 2.16: Steps to obtain the cranial implant geometry [Moiduddin *et al.* 2017].

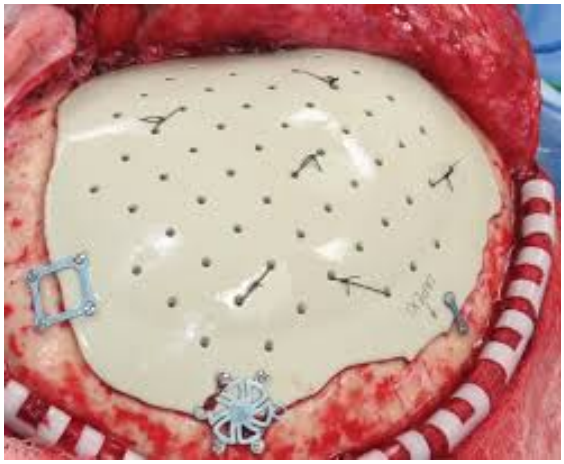

Figure 2.17: Small holes incorporated at the implant [Rosenthal *et al.* 2014].

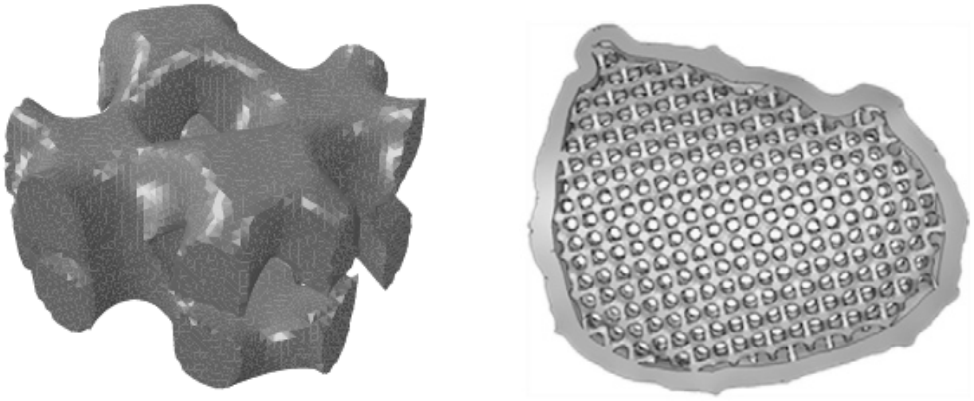

(a) Typical scaffold pattern.

(b) Cranial implant with a scaffold structure.

Figure 2.18: Application of CAD techniques to obtain a scaffold structure from a pattern design [El Halabi *et al.* 2011].

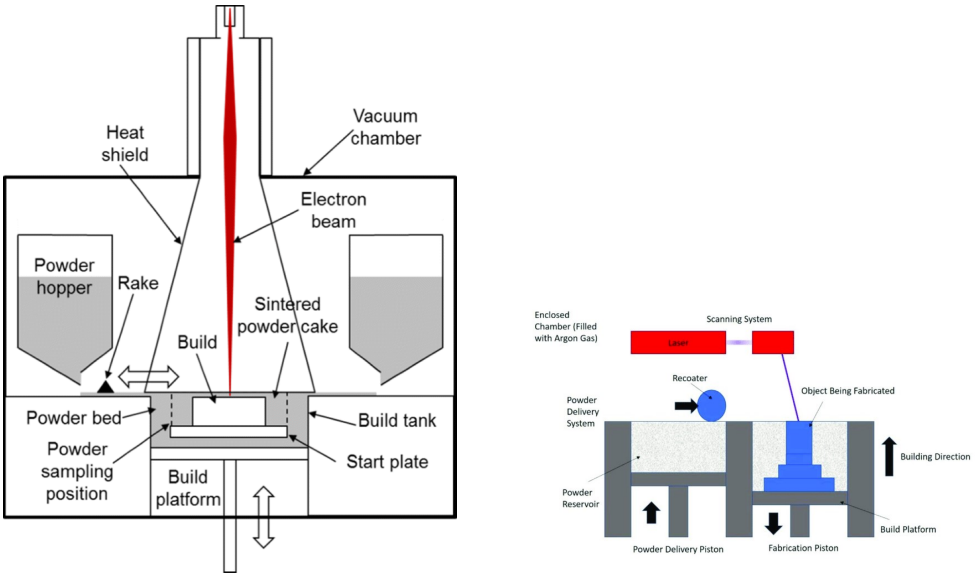

(a) Scheme of the EBM process.

(b) Scheme of the SLM and SLS process.

Figure 2.19: Representation of the most common AM techniques to obtain cranial implants.

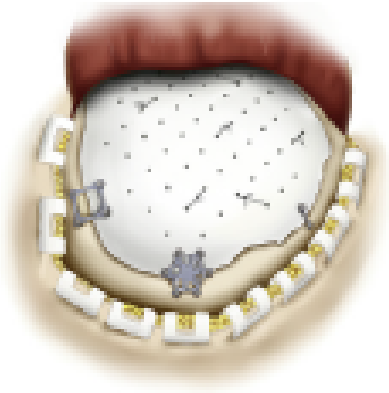

Figure 2.20: Titanium miniplates as the fixation method [Zhang *et al.* 2019].

Figure 2.21: Tangential screws as the fixation method [Xilloc 2021b].

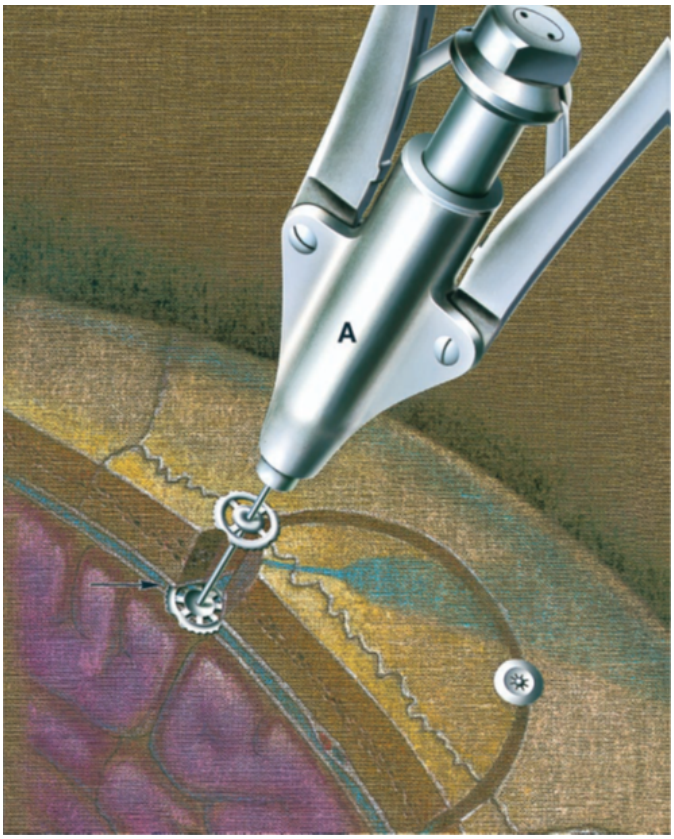

Figure 2.22: Titanium clamps as the fixation method [Estin *et al.* 2000].

2.4 Finite Element Analysis of Cranial Implants

Different strategies, different software and different methodologies have been employed to validate the developed models of cranial implants. This is perhaps the most important step of the mechanical resistance study and all the assumptions made have a huge impact on the approximation made by the finite element analysis (FEA).

2.4.1 Evaluation of Patient-Specific Cranial Implant Design Using Finite Element Analysis

Huys et al. [Huys *et al.* 2021] used the software Abaqus (Dassault Systèmes, France) to run a FE analysis on three different models with similar strategies addopted: a PEEK cranial implant fixed with tangential screws and 2 ceramic-titanium (CeTi) cranial implants fixed with tangential and axial screws (Fig. 2.23).

In this study, the complete head model was not used, instead, to reduce the computational cost, only the part of the skull surrounding the defect was taken into account. All material properties were considered to be linear elastic and the contact between the different parts (implant and bone) was assumed to occur only at the screw holes, with complete fixation assumed as tangential or axial screws were the chosen fixation method. This assumptions were modeled in Abaqus using *hard contact* interaction property and the *tie constrain* [Huys *et al.* 2021].

Two static loads were applied to the model: one being an impact load due to a fall off a bicycle, applied as a pressure perpendicular to a circular area, and the other one being an internal pressure evenly distributed over the inner surface of the implant (representing the elevated intracranial pressure). Since it was assumed that the caudal side of the neurocranium is completely anchored, the boundary condition *Encastre* was employed to constrain translation and rotation in all directions [Huys *et al.* 2021].

Results showed that PEEK offer inferior brain protection as a result of its high flexibility and local peak stresses at the bone-screw interface. On the other hand, CeTi implants appeared to have a better potential to protect the brain since it was able to distribute the stress along the surface [Huys *et al.* 2021].

2.4.2 The Potential of The Three-dimensional Printed Titanium Mesh Implant For Cranioplasty Surgery Applications: Biomechanical Behaviors and Surface Properties

In order to study the biomechanical behaviour of titanium mesh cranial implants with different thicknesses, pore structures and surface characteristics, Huang et al. [Huang *et al.* 2019] executed the FE analysis using the software ANSYS work bench 12.1. Also, all material properties were treated as linear elastic, isotropic and homogeneous. The mesh of both implant and cortical bone was built with tetrahedral elements with 10 nodes [Huang *et al.* 2019].

The skull was fixed in the bottom (Fig. 2.24), where all rotations and translations were constrained, and a static load of 50 N was placed in the center of the implant (Fig. 2.24) to mimic the weight of the human head. Thus, to overcome the presence of the screws and the complexity of those in the numerical simulation, the ANSYS boned contact algorithm was used instead, neglecting the stress of the screws. Moreover, the movement between implant and bone was not allowed [Huang *et al.* 2019].

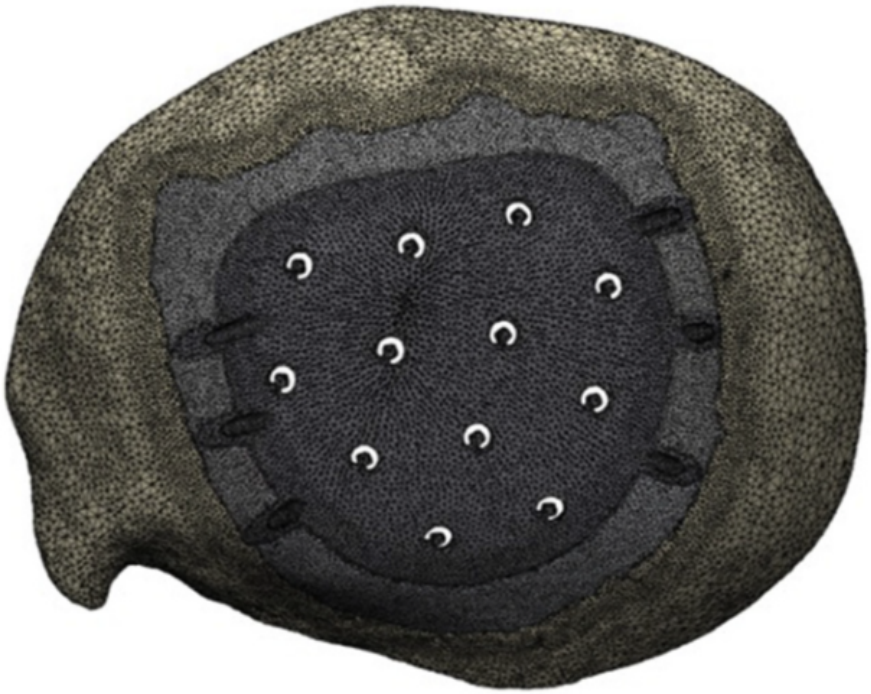

Figure 2.23: CeTi implant mesh, with tangential screws as the fixation method [Huys *et al.* 2021].

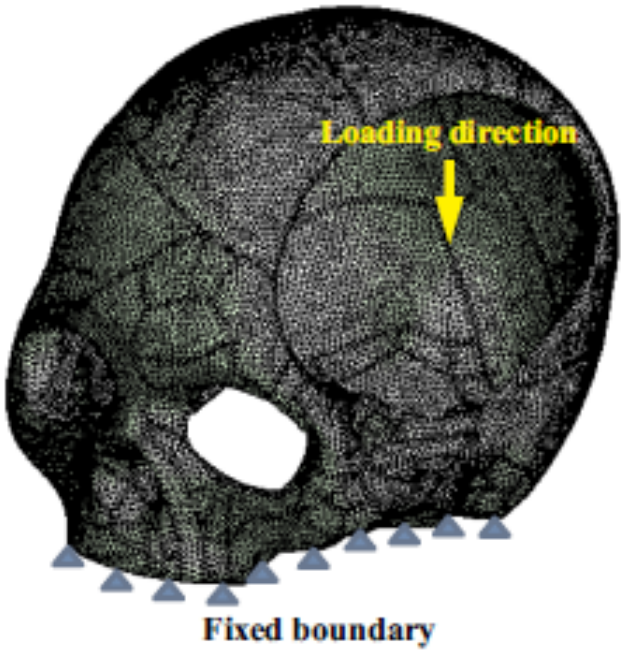

Figure 2.24: Load and boundary conditions of the model [Huang *et al.* 2019].

Finally, results of the analysis showed that the stress distribution and peak von Mises stress of the implants decreases at the thickness of 1 milimeter. Also, implants with a circular pore pattern results in a lower von Mises stress on the bone defect area when compared with triangular and square pore pattern [Huang *et al.* 2019].

2.4.3 On The Mechanical Behaviour of PEEK and HA Cranial Implants Under Impact Loading

To compare the mechanical impact response of PEEK and hydroxyapatite (HA), a study was carried on by Garcia-Gonzalez et al. [Garcia-Gonzalez *et al.* 2017] performing explicit analysis on the software Abaqus. A quite complex FEHM was used, containing scalp, skull, cerebral falx, CSF and brain tissues, all developed from MRI, with the main goal being the implant performance and capacity to prevent failure and TBI.

Constitutive models for different parts of the human head were employed based on a selection from the literature, while for PEEK a constitutive model previously developed by the authors was addopted. Even though the scalp has been proposed with a hyperelastic constitutive model, in this work it was modelled as a rate-independent, isotropic, homogeneous and linear elastic as a simplification, due to the high computational cost of the numerical simulations involving a full head model. The properties used for scalp are identified int Table 2.3 [Garcia-Gonzalez *et al.* 2017].

Skullbone and falx were also modelled as an isotropic, homogeneous and linear elastic material even though skullbone is a complex anisotropic composite. To reproduce the role of the two external layers of cortical bone and the internal layer of trabecular bone, a homogenised Young's modulus has been employed. Mechanical properties for the skullbone and falx are shown in Table 2.4 [Garcia-Gonzalez *et al.* 2017].

Even though CSF is considered by many authors to be a linear elastic material, in this work a more complete constitutive model is adopted considering its similarity with water in terms of viscosity. The mechanical properties designated for the CSF are introduced in Table 2.5 [Garcia-Gonzalez *et al.* 2017].

Last but not least, the brain tissue were assigned a unique set of properties for both gray and white matters, even though they behave differently. Also, the viscoelastic behavior has been taken into account. Brain tissues mechanical properties are shown in Table 2.6 [Garcia-Gonzalez *et al.* 2017].

As mentioned previously, a constitutive model developed, calibrated and validated by the authors was employed to describe PEEK mechanical behavior. A hyperelastic-thermoviscoplastic constitutive model is defined taking into account pressure dependency and strain rate and temperature sensitivities. Table 2.7 contains the constants that defines the material model.

In the numerical model, the contact was modeled with a penalty contact algorithm with a friction coefficient of 0.4. Since the model does not include screws, a parallel analysis was developed in order to capture the stress concentration introduced by the

Table 2.3: Material properties which define the scalp on FEHM developed by Garcia-Gonzalez et al. [Garcia-Gonzalez *et al.* 2017].

ρ (ton/mm^3)	ν	E (MPa)
1.1×10^{-9}	0.42	16.7

Table 2.4: Material properties which define the skullbone and falx on FEHM developed by Garcia-Gonzalez et al. [Garcia-Gonzalez *et al.* 2017].

Tissue	ρ (ton/mm^3)	ν	E (MPa)
Skullbone	1.728 $\times 10^{-9}$	0.22	8000
Falx	1.133 $\times 10^{-9}$	0.45	31.5

Table 2.5: Material properties which define the CSF on FEHM developed by Garcia-Gonzalez et al. [Garcia-Gonzalez *et al.* 2017].

ρ (ton/mm^3)	c_0 (mm/s)	s	Γ_0	η (MPa s)
1 $\times 10^{-9}$	1.45 $\times 10^{6}$	1.99	0.11	8.9 $\times 10^{-10}$

Table 2.6: Material properties which define the brain tissues on FEHM developed by Garcia-Gonzalez et al. [Garcia-Gonzalez *et al.* 2017].

ρ (ton/mm^3)	Bulk Modulus (MPa)	G_0 (MPa)	G_∞ (MPa)	β (s$^-$1)
1.04 $\times 10^{-9}$	2190	0.528	0.168	35

Table 2.7: Material properties PEEK developed by Garcia-Gonzalez et al. [Garcia-Gonzalez *et al.* 2017].

Initial elastic properties					
E_{ref} (MPa)	E_1 (MPa)	ν	$\dot{\varepsilon}_{0A}$ (s$^-$1)	C	
3.2	-3.0	0.4	0.001	0.38	
Intermolecular resistance					
σ_{T0} (MPa)	m	θ_{ref} (K)	θ_{melt} (K)	α	β
108	0.69	296	612	1.2	1.0
General properties					
ρ (ton/mm^3)		$\overline{C}$ (mJ/mm^{3}K)		α_θ (K^{-1})	
1.3 $\times 10^{-9}$		2.83 $\times 10^{6}$		4.6$\times 10^{-6}$	
Network resistance					
C$_R$ (MPa)		$\overline{\lambda}_L$		κ	
0.4		5.5		0.0	

screws. After, this stress concentration factor, found to have a value of 1.28, was applied to the surrounding of the screws [Garcia-Gonzalez *et al.* 2017].

A set of numerical simulations were carried on to study the mechanical response of the FEHM for an impact velocity varying from 1 m s^{-1} to 7 m s^{-1} including three different scenarios: a FEHM including a PEEK implant, a FEHM including a HA implant and a FEHM including no defect. The results were analysed on three different categories: acceleration-time predictions, critical impact velocity predictions, and TBI predictions. For this purpose, only the results obtained for critical impact velocity predictions for the model with a PEEK implant will be reported [Garcia-Gonzalez *et al.* 2017].

With regard to the implant failure during an impact, the impact velocity and the impact location have been considered as variables. So a parametric study was performed varying both variables along three paths to reach the most common impact scenarios in fall accidents. These paths are: from parietal bone to vertex, from parietal bone to occipital bone, and from parietal bone to frontal bone. Fig. 2.25(b) contains the critical impact velocity that results in implant failure depending on the distance from the interface for each path [Garcia-Gonzalez *et al.* 2017].

For all paths, the most critical zone is the interface between implant and bone where the screws are located, while the weakest path is the parietal-vertex. Another conclusion taken from this study is that the critical impact velocity resulting in implant failure when the impact occurs far from the peripheral zone is a good indicator of the material mechanical properties and load-bearing capacity, once the effect of screws can be neglected [Garcia-Gonzalez *et al.* 2017].

2.5 Human Head Model

The base human head model used in this dissertation is YEAHM (YEt Another Head Model), initially developed by Fernandes et al. [Fernandes *et al.* 2018] and afterward ameliorated by Migueis et al. [Migueis *et al.* 2019], Costa et al. [Costa *et al.* 2020] and Barbosa et al. [Barbosa *et al.* 2020]. The initial model was composed only of a skull, brain and CSF (Fig. 2.26), while the inclusion of the bridging veins (BV) and superior sagittal sinus (SSS) being a significant alteration of the enhanced models (Fig. 2.27).

In the original model, the bone that makes up the skull was homogeneous and did not feature the distinction between cortical bone, trabecular bone or cranial sutures. These details were only added by Barbosa et al. [Barbosa *et al.* 2020], increasing significantly the level of verisimilitude of the model.

The material of the brain was modeled as hyper-viscoelastic, the CSF was considered to be a hyperelastic material and the SSS and BV were modeled with an elastoplastic law [Fernandes *et al.* 2018]. In the original model, the homogeneous skullbone was defined as linear elastic model, but in Barbosa et al. [Barbosa *et al.* 2020] enhanced model all the bone types were individually defined: the trabecular bone as elastic-plastic material - Fig. 2.28 shows the stress-strain curve and Table 2.11 the elastic properties used to define the trabecular bone material model - while cortical bone and cranial sutures were treated as a quasi-brittle material model - Table 2.11 contains the elastic properties and Fig. 2.29 and Fig. 2.30 shows the values used with respect to crack initiation and the behavior of bone tissue after cracking, and the shear retention model, respectively [Barbosa *et al.* 2020].

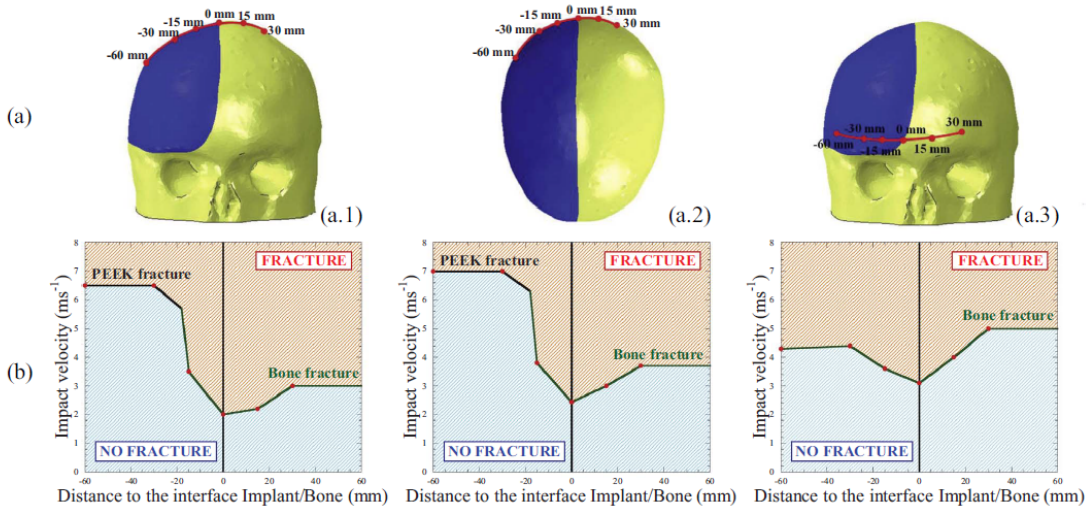

Figure 2.25: (a) Impact localisation points defined along the three skull paths studied: (a.1) parietal-vertex; (a.2) parietal-occipital; and (a.3) parietal-frontal. (b) Risk of fracture as a function of impact velocity and distance to the implant interface along different paths for PEEK implant [Garcia-Gonzalez *et al.* 2017].

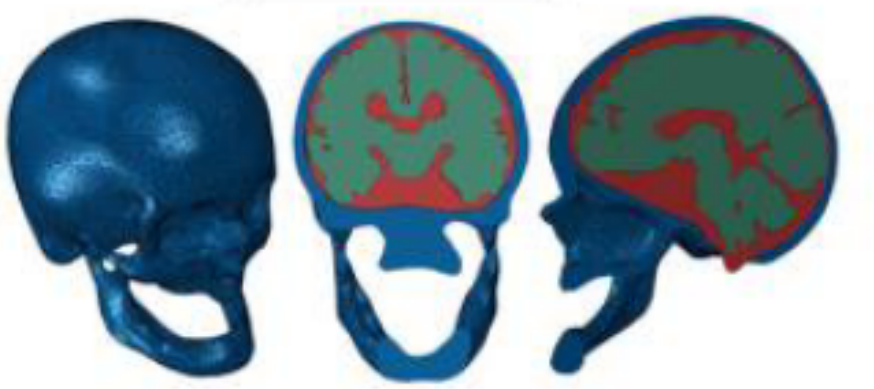

Figure 2.26: Original YEAHM containing the skull, brain and CSF [Fernandes *et al.* 2018].

Figure 2.27: New head model containing the skull, brain, CSF, SSS and BV [Barbosa *et al.* 2020].

Table 2.8: Material properties which define the brain (hyper-viscoelastic model) [Fernandes *et al.* 2018].

ρ (ton/mm^3)	$\mu(MPa)$	α_1	D_1 (MPa^{-1})	g_1	g_2	τ_1 (s)	τ_2 (s)
1.04 $\times 10^{-9}$	0.012	5.0507	0.04	0.5837	0.2387	0.02571	0.0257

Table 2.9: Material properties that define the CSF (hyperelastic model) [Fernandes *et al.* 2018].

ρ (ton/mm^3)	C_10	C_01	D_1 (MPa^{-1})
1.0 $\times 10^{-9}$	0.9	1	0.9

Table 2.10: Material properties which define the BV's and SSS (elastoplastic) [Barbosa *et al.* 2020].

E (MPa)	ν	Fracture Strain	Stress Triaxiality	Strain Rate (s^{-1})	Displacement at failure
25.72	0.45	0.31875	0.33	135.86	0.05

Table 2.11: Elastic properties of the cortical bone, trabecular bone and sutures [Barbosa *et al.* 2020].

Tissue	ρ (ton/mm^3)	E (MPa)	ν
Cortical	1.9 $\times 10^{-9}$	20000	0.21
Trabecular	1.5 $\times 10^{-9}$	1000	0.05
Sutures	2.1 $\times 10^{-9}$	15000	0.3

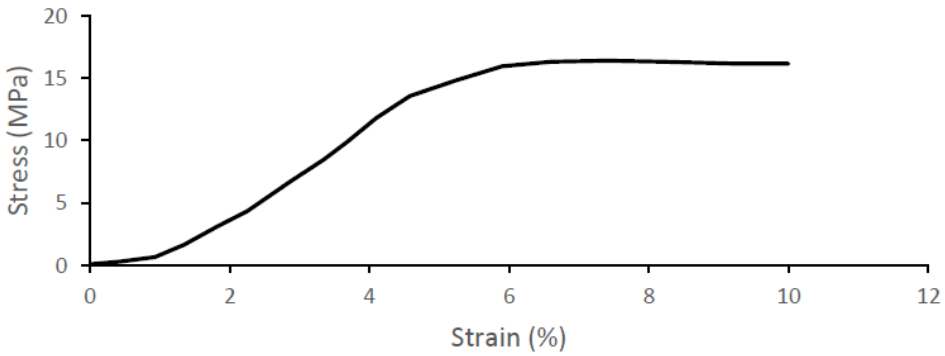

Figure 2.28: Stress-strain curve used to define trabecular bone [Barbosa *et al.* 2020].

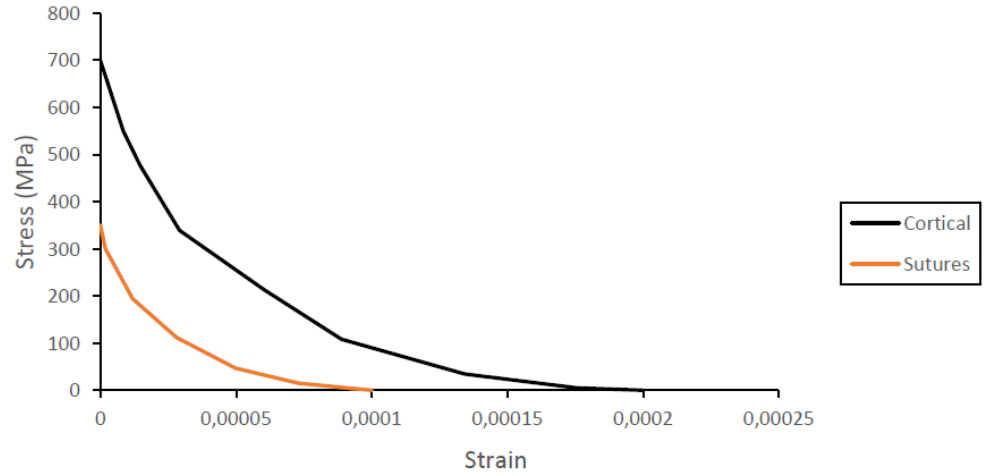

Figure 2.29: Post-failure stress-strain curve for cortical and sutures [Barbosa *et al.* 2020].

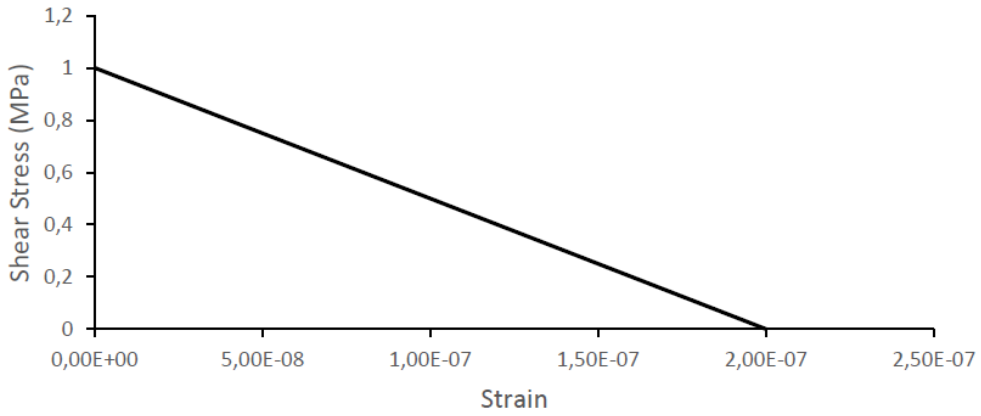

Figure 2.30: Shear retention model values for cortical and sutures tissues [Barbosa *et al.* 2020].

The boundary conditions of the model include finite-sliding formulation interactions and kinematic contact between the CSF and the brain and between the CSF and the skull, with a coefficient of friction for tangential behavior of 0.2 [Fernandes *et al.* 2018].

The YEAHM mesh contains a total of 1033976 elements, with 836328 elements belonging to the brain, 57257 elements to the skull, 98032 to the CSF and 42359 elements for the SSS + BV set. Instead of using the typical C3D4 tetrahedral elements, second-order C3D10M are used because these elements are more suitable for contact situations and are more robust in situations of volumetric retention. Furthermore, with the skull alterations made by Barbosa et al. [Barbosa *et al.* 2020], the final model which acts as a start point for this work contemplates 237616 hexahedral elements for the skull, of which 92300 is for the trabecular bone, 133045 for the cortical bone and 12271 for the cranial sutures.

Intentionally blank page.

Chapter 3

Implant Material

3.1 Chosen Implant Material

Based on the arguments presented in Chapter 2, Section 2.2, Subsection 2.2.5, the material chosen for the implant is PEEK. In order to define the material model, a work presented by Garcia-Gonzalez et al. [Garcia-Gonzalez *et al.* 2015] was taken into account and will be explained in this chapter. This material model presents a more complete and suitable solution to define the material, including damage, dynamic behavior and interesting thermo mechanical phenomena reported for PEEK. So, unfilled PEEK 450G, general purpose grade, was the material modeled and associated with the implant.

3.2 Modeling the Behaviour of PEEK 450G

3.2.1 Viscoplasticity

Based on the work developed by Garcia-Gonzalez et al. [Garcia-Gonzalez *et al.* 2015], the material model in this work adopts the Jonhson and Cook (JC) model. This approach is justified by the strain rate and temperature sensitivity of PEEK observed in Fig. 3.1, which indicates a viscoplastic behavior.

Although JC model is regularly applied to ductile metal alloys, it was already applied to polymers [Louche *et al.* 2009]. It is frequently used in finite element codes, including explicit analysis in Abaqus. The strength model can be described as

$$\overline{\sigma}(\overline{\varepsilon}^p, \dot{\overline{\varepsilon}}^p, T) = [A + B \times (\overline{\varepsilon}^p)^n] \left[1 + C \times \ln\left(\frac{\dot{\overline{\varepsilon}}^p}{\dot{\overline{\varepsilon}}^p_n}\right)\right] [1 - \Theta^m] \tag{3.1}$$

where A is the yield strength at quasi-static strain rate, B and n represent the influence of the strain hardening, m is the temperature sensitivity, T_0 is the initial temperature and T_m is the melting temperature while the first term is the strain hardening $\overline{\varepsilon}^p$, the second one is the strain rate sensitivity $\dot{\overline{\varepsilon}}^p$ and the third one is related to thermal softening Θ, where

$$\Theta = \frac{T - T_0}{T - T_m}. \tag{3.2}$$

In order to obtain the temperature increment in adiabatic conditions, the equation

$$\Delta T(\overline{\varepsilon}^p, \dot{\overline{\varepsilon}}^p, T_0) = \frac{\beta}{\rho \times C_p} \int_{\varepsilon}^{\overline{\varepsilon}^p} \overline{\sigma}(\overline{\varepsilon}^p, \dot{\overline{\varepsilon}}^p, T) d\overline{\varepsilon}^p \tag{3.3}$$

allows us to do it, with ΔT being the temperature increment, T_0 the room temperature, β the Quinney–Taylor heat fraction coefficient, ρ the material density and C_p the specific heat at constant pressure. In this work, the author assumed the Quinney–Taylor heat fraction coefficient β to be constant and equal to 0.9.

As reported by Garcia-Gonzalez et al. [Garcia-Gonzalez *et al.* 2015], all these parameters were determined by analyzing the results of the various compressive tests at various strain rates and temperatures (Fig. 3.1) [Rae *et al.* 2007] following methodologies reported for ductile metals and polymers. So, parameters A, B and n were determined by tests at room temperature, parameter C was identified by Eq. 3.4 with different strain rates and null plastic strain ($\overline{\sigma} = \overline{\sigma}_y$) at room temperature. Thus, the temperature sensitivity parameter m was determined by Eq. 3.5 for a range of temperatures, varying from the initial temperature to the melting temperature.

$$C = \frac{\overline{\sigma}_y - A}{A \times \ln\left(\frac{\dot{\overline{\varepsilon}}^p}{\dot{\overline{\varepsilon}}^p_0}\right)} \tag{3.4}$$

$$m = \frac{1 - \frac{\overline{\sigma}}{(A + B \times (\overline{\varepsilon}^p)^n)}}{\ln\left(\frac{T - T_0}{T - T_m}\right)} \tag{3.5}$$

Table 3.1 contains the constants used to define the material behavior, in other words, the JC parameters. To prove the accuracy of this model, Fig. 3.2 shows the comparison between the experimental data [Rae *et al.* 2007] and this JC model [Garcia-Gonzalez *et al.* 2015], both at different strain rates and room temperature.

3.2.2 Fracture Model

As reported by Garcia-Gonzalez et al. [Garcia-Gonzalez *et al.* 2015], the fracture model is essential to a more robust and complete model, so a fracture model proposed by Johnson and Cook [Johnson and Cook 1985] was used. This proposal includes strain hardening, strain rate, temperature and stress triaxiality, a very important factor to define PEEK. For this model, already employed in ductile metal alloys and semicrystalline polymers, failure is assumed when a D parameter surpass unity. The evolution of D can be described as

Table 3.1: Properties used to define the thermoviscoplastic behavior of PEEK 450G at high strain rates in adiabatic conditions [Garcia-Gonzalez *et al.* 2015].

Thermoviscoplastic behavior					
A (MPa)	B (MPa)	n	$\dot{\overline{\varepsilon}}^p_0$ (s$^-$1)	C	m
132	10	1.2	0.001	0.034	0.7
Elasticity		**Other physical constants**			
E_0 (MPa)	ν	ρ (ton/mm^3)	β	C_p (mJ/ton K)	T_m (K)
3600	0.4	1.3 $\times 10^{-9}$	0.9	2.18 $\times 10^{9}$	614

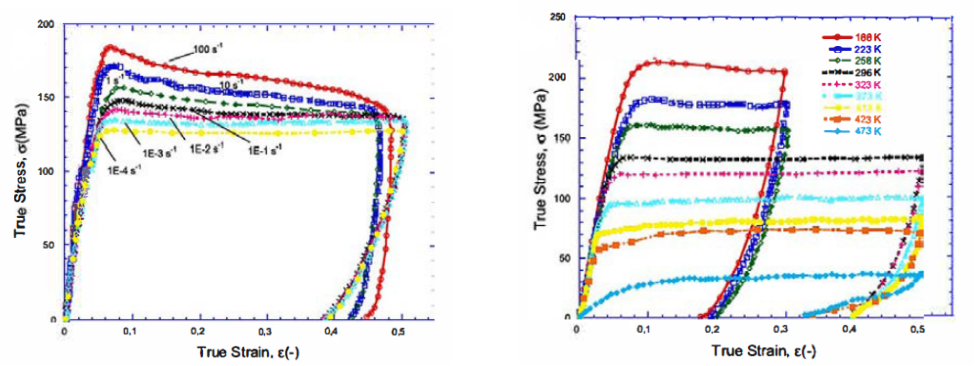

(a) Strain sensitivity.

(b) Temperature sensitivity.

Figure 3.1: Mechanical behavior of PEEK under compression for (a) different strain rates under room temperature and (b) different temperatures under a strain rate of 0.001 s^{-1} [Rae *et al.* 2007].

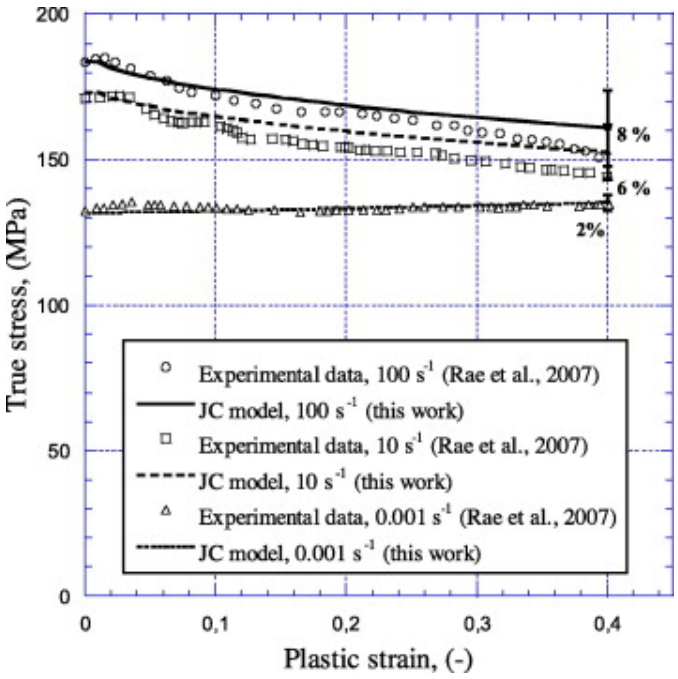

Figure 3.2: Stress-strain values of PEEK 450G according to experimental data [Rae *et al.* 2007] and JC model [Garcia-Gonzalez *et al.* 2015].

Table 3.2: Fracture constants [Garcia-Gonzalez *et al.* 2015].

D_1	D_2	D_3	D_4	D_5
0.05	1.2	0.254	0.009	1.0

$$D(\bar{\varepsilon}^p, \dot{\bar{\varepsilon}}^p, T) = \sum \frac{\Delta\bar{\varepsilon}^p}{\bar{\varepsilon}^p_f(\dot{\bar{\varepsilon}}^p, T, \sigma^*)} \tag{3.6}$$

where $\bar{\varepsilon}^p$ is an increment of accumulated plastic strain over an integration cycle and $\bar{\varepsilon}^p_f$ is the critical failure strain level [Garcia-Gonzalez *et al.* 2015]. Since this type of fracture model leads to an element deletion in Abaqus when an indicated strain level is reached, the mesh must be very refined in the interest zone in order to mitigate the negative effect on the numerical results in terms of energy [Garcia-Gonzalez *et al.* 2015]. Next, the plastic failure strain $\bar{\varepsilon}^p_f$ is dependent on a plastic strain rate $\dot{\bar{\varepsilon}}^p/\dot{\bar{\varepsilon}}^p_0$, a dimensionless pressure deviatoric stress ratio σ^* and a non dimensional temperature Θ [Garcia-Gonzalez *et al.* 2015]. Eq. 3.7 shows these dependencies with D_i being failure constants.

$$\bar{\varepsilon}^p_f = [D_1 + D_2 \times \exp(D_3 \times \sigma^*)] \left[1 + D_4 \times \ln\left(\frac{\dot{\bar{\varepsilon}}^p}{\dot{\bar{\varepsilon}}^p_0}\right)\right] [1 + D_5 \times \Theta] \tag{3.7}$$

D_1 assumes a finite strain to fracture even at very high values of stress triaxiality. Garcia-González et al. [Garcia-Gonzalez *et al.* 2015] indicated a value of $D_1 = 0.5$. On the other hand, D_2 and D_3 are determined based on experimental data [Rae *et al.* 2007] of tensile tests of unnotched specimens of PEEK 450G at strain rate equal to 0.001 s^-1 and room temperature. The constants D_4 and D_5 are determined based on experimental data of uniaxial tests [Sobieraj and Rimnac 2012] of unnotched specimens of PEEK 450G at different strain rates and temperatures. Table 3.2 contains the values of the fracture constants.

Chapter 4

Methodology

4.1 Skull Defect Creation and New Mesh

First of all, the head model previously mentioned was used and manipulated with the software Hypermesh (Altair, USA) in order to obtain the skull model after the craniectomy. The option was to create a large skull defect with approximately 50 cm^2 at the parietal zone to reproduce a plausible situation. Then, nodes were selected, performing an approximated contour of the implant at the desired skull location, and used to create a spline surface which acted as a start point to obtain the skull defect and the implant.

Once this surface was completed, it was used to create the defect in the skull to place the implant. The skull elements intersecting this surface along the thickness were deleted (Fig. 4.1) and then, in order to smooth the skull defect contour, the border elements were projected to this surface (Fig. 4.2).

Then, the model of the skull was exported to Abaqus and, using the tool *Verify mesh* from Abaqus toolbox some elements with extremely low volume (near zero) on the defect's border were identified and eliminated, so the analysis could be performed. Figure 4.3 contains different views over the skull's final mesh.

Overall, the skull's new mesh contains a total of 223401 linear hexahedral elements of type C3D8R, of which 124714 are from cortical bone, 86703 from trabecular bone and 11984 from cranial sutures.

4.2 Implant Geometry and Mesh

The surface obtained previously when creating the hole in the skull was given a thickness of 4 millimeter, decision made based in previous studies [Marcián *et al.* 2019], where the influence of different thicknesses was evaluated using FEM under three loading scenarios. The implant thickness contains a chamfer to facilitate the assembly in the skull. For the reasons mentioned in Chapter 2, Section 2.3, Subsection 2.3.2, 28 holes with 2 millimeter size were incorporated in the implant.

The process of meshing the implant was performed with the software Hypermesh (Altair, USA). Firstly, a 2D mesh was created on the exterior surface of the implant with square elements of approximately 1.2 millimeter size (Fig. 4.4). Next, an offset was made in order to create 3D elements. This offset consisted of four layers along with the

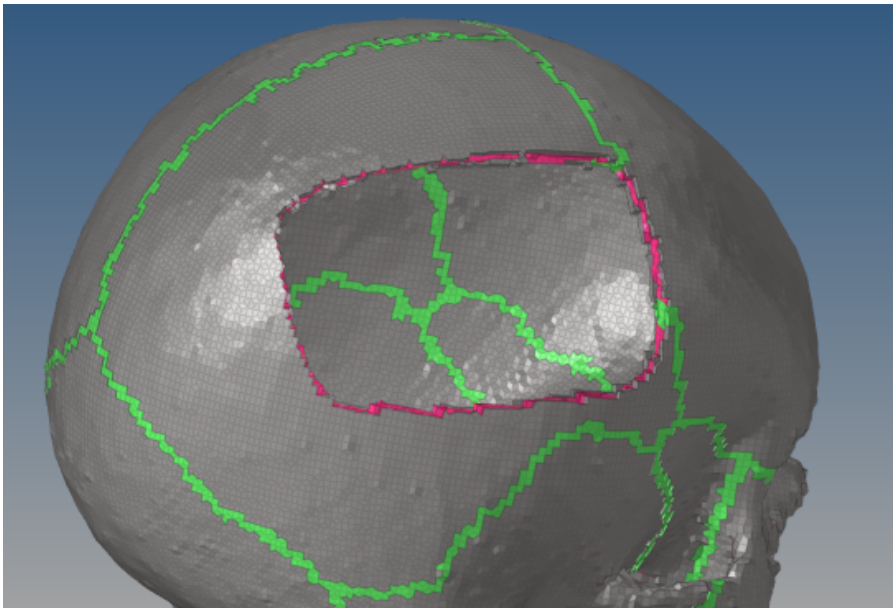

Figure 4.1: Initial skull defect, obtained by eliminating elements.

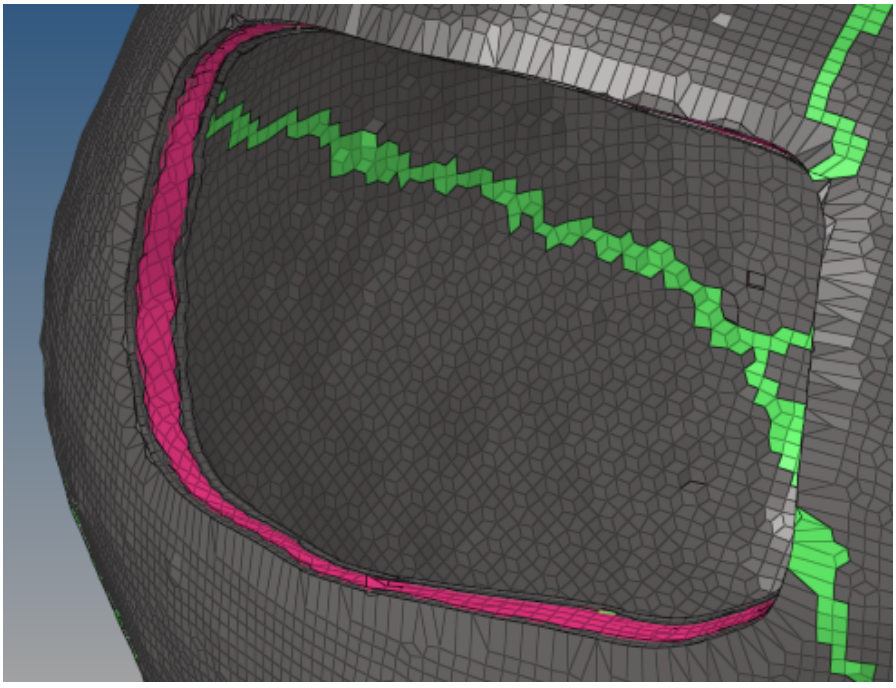

Figure 4.2: Skull defect after border elements have been projected.

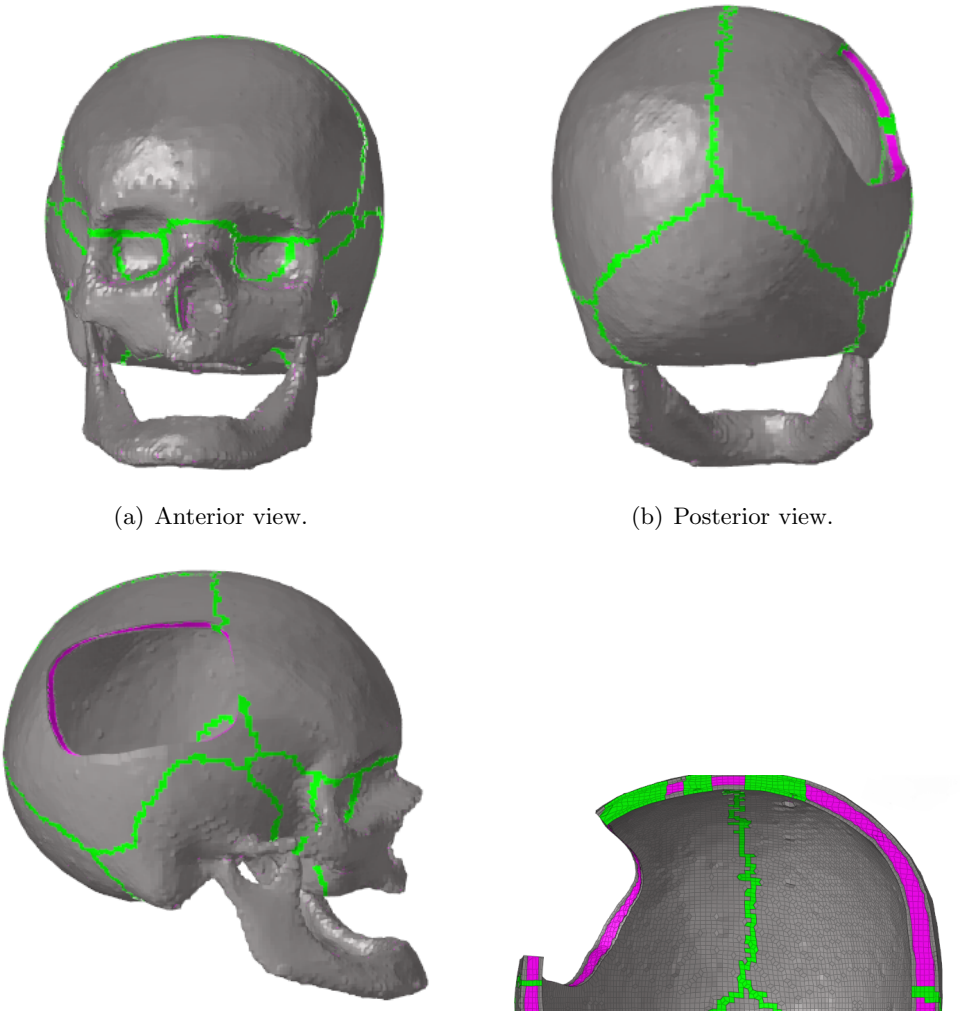

(a) Anterior view.

(b) Posterior view.

(c) Lateral view.

(d) Cut view of the skull defect.

Figure 4.3: Different views over the skull mesh.

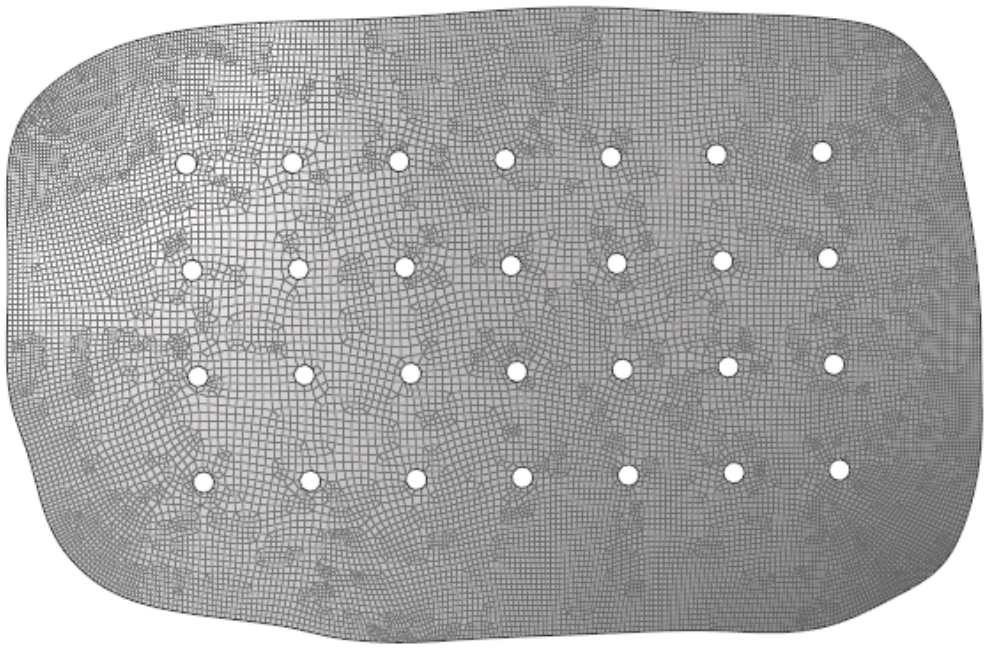

Figure 4.4: 2D mesh on the exterior surface of the implant.

thickness of the implant, each layer with 1 millimeter size (Fig. 4.5).

Since the geometry is not very complex, linear hexahedral elements were used to perform the mesh of the implant given the fact that it allows for more accurate results. Also, reduced integration was employed in order to reduce the computational cost. Overall, the implant mesh contains a total of 20940 C3D8R elements and 27285 nodes.

4.3 Interaction

4.3.1 Interaction Type

Based on what was assumed on the head model used in this work [Barbosa *et al.* 2020], a frictionless general contact between all parts is maintained in this model because the tangential behavior is not the most relevant in the studies carried on and also to ease the computational cost.

4.3.2 Fasteners

Based on what was explained previously, the chosen fixation method in this work was tangential screws, given the fact that allows for a more rigid connection and it's aesthetically more suitable. Since modeling the geometry of the screws, their material properties and their interaction with the other parts is a hard task, the option was to employ the tool *Fasteners* from the Abaqus toolbox to represent the effect of the screws. This tool consists in a mesh-independent connection between surfaces, that

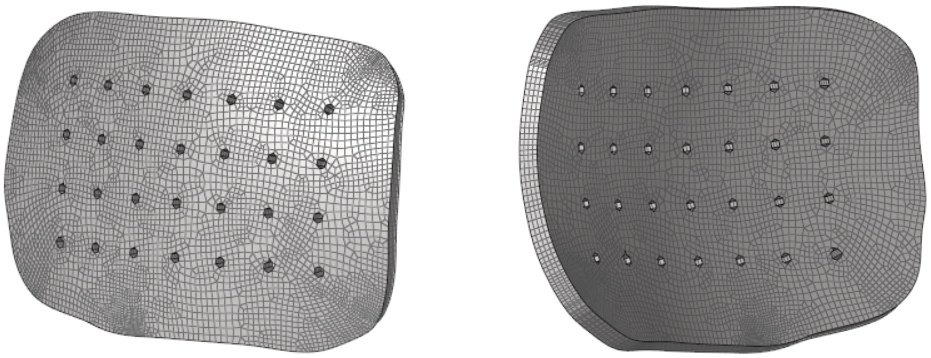

(a) Exterior surface of the implant mesh. (b) Interior surface of the implant mesh.

Figure 4.5: Different views over the implant mesh.

connects two or more parts by using attachment lines and connectors, that define the fastener location. These attachment lines are created by projecting the reference point to the closest surfaces selected. Also, the connection between the connector and the nodes located nearby is accomplished by coupling the displacement and rotation of the connector element nodes and the average displacement and rotation of the nodes located inside a radius of influence. The radius of influence assigned was 1 millimeter.

With regard to the properties of the *Fasteners* tool, Korolija [Korolija 2012] made a parametric study to find out the best connector type to be associated to the attachment lines and the mechanical behavior which best represented titanium screws. So, in Abaqus, there are different ways to represent the fasteners, such as:

1. Beam elements;
2. Connector elements;
3. Rigid elements;
4. Solid elements;
5. Spring elements.

In the study performed, the author opted for analyzing only beam elements and connector elements. Beam elements are reported to work well with geometries modeled with shell elements, but when it comes to solid elements, it can be problematic due to the lack of rotational degrees of freedom [Korolija 2012]. This happens because both shell and beam elements have six degrees of freedom (three translational and three rotational) while solid elements have no rotational degrees of freedom [Korolija 2012]. Also, there are multiple types of connector elements with different characteristics, and in this study [Korolija 2012] bushing elements were used. Figure 4.6 shows the behavior of the bushing elements due to secondary bending.

Further, elasto-plastic constitutive behavior was given to the connector element, based on experiments made by Huth [Huth 1983], assigning force-displacement characteristics. Tables 4.1 and 4.2 include the values from elastic behavior and plastic behavior, respectively, defined by Huth's [Huth 1983] experiment.

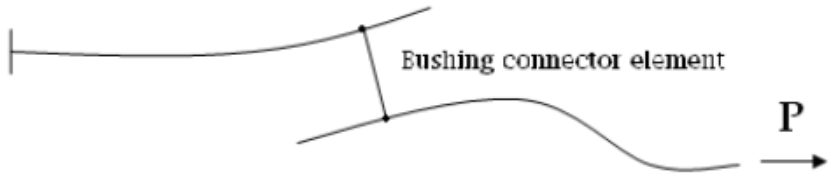

Figure 4.6: Behaviour of bushing connector elements due to secondary bending [Korolija 2012].

Table 4.1: Linear elastic constitutive behaviour of the connector elements based on Huth's experiments [Huth 1983].

Applied stiffness in the load direction [N/mm]	**All the other directions**
185051	Rigid

Table 4.2: Plastic constitutive behaviour of the connector elements based on Huth's experiments [Huth 1983].

Force (each screw) [N]	**Relative plastic displacement [mm]**
1000	0.000
2000	0.005
4000	0.020
6000	0.080
9000	0.225
11000	0.400
13000	0.640

In order to define the number of screws and their diameter, the advices of the *InterFix* technology [Xilloc 2021a] was employed. This technology recommends the use of 5 to 9 screws for a large implant, so, further, in this work, a parametric study will be carried on in order to find out the best configuration of the screws. Still, Fig. 4.7 shows an example of the configuration with 9 screws.

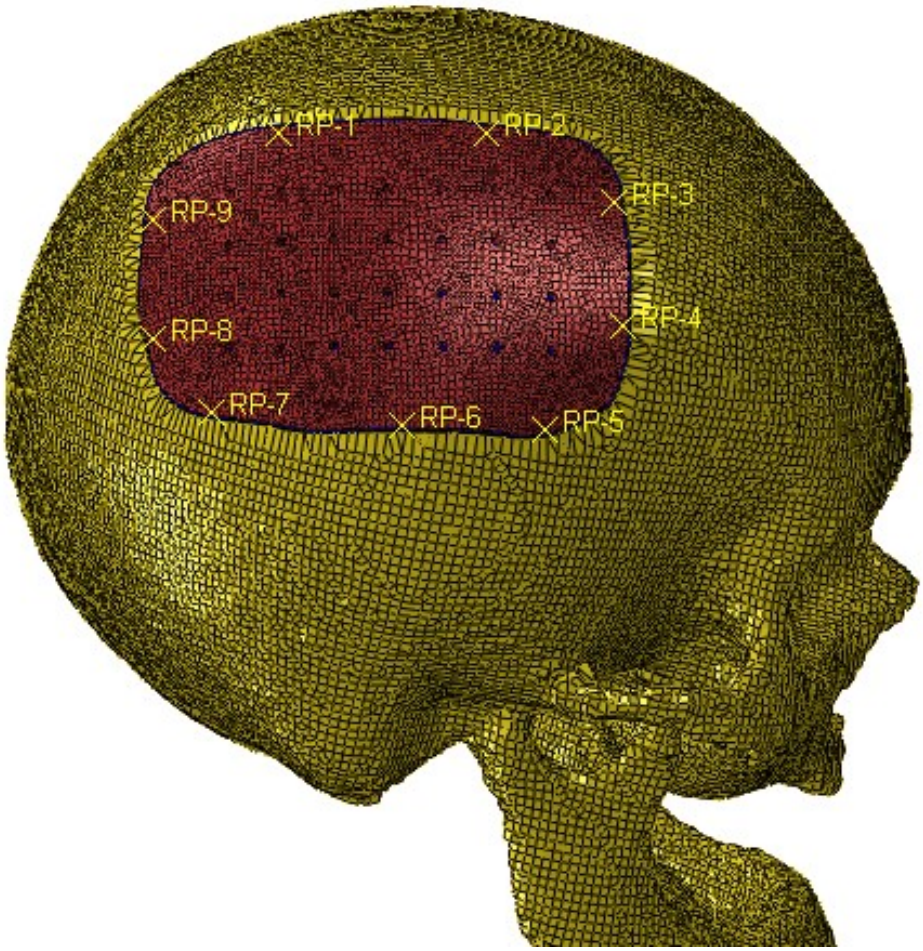

Figure 4.7: Position of the screws, represented by the reference points (RPs).

4.4 Head Model + Implant

Once completed the previous steps of creating the skull defect and the implant mesh, all parts (brain, BVs and SSS, CSF, skull and implant) were assembled on Abaqus in order to get the model ready for further numerical simulations. This assembly contains a total of 1208740 elements and can be seen in Figure 4.8.

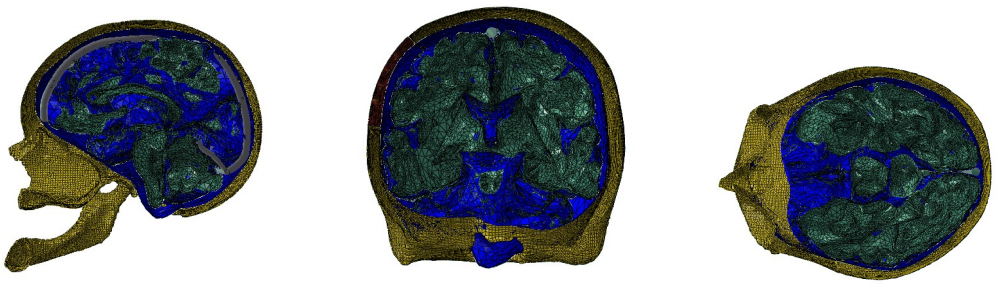

(a) Sagittal view. (b) Frontal view. (c) Transverse view.

Figure 4.8: Different cut views of the assembly.

Chapter 5

Numerical Simulations and Results

With the aim of testing the load bearing capacity of the model Head + Implant developed previously, numerical studies were carried out using FEM. All the numerical simulations were dynamic explicit analysis, which allows solving problems associated with complex deformable bodies. Theoretically, the computational cost of an increment in explicit analysis is lower than in implicit analysis, however, time increments in explicit analysis have to be very small so the stability of the method and reliability of the solution are maintained.

All the impacts simulated were representative of falls, so a rigid plate, modeled as an analytical rigid part, was assembled on the model simulating the ground. Also, instead of defining the velocity on the head model, this was defined as a predefined field on the rigid plate and the head model had no boundary conditions. Also, a mass of 0.001 tons was given to the rigid plate. Figure 5.1 shows an image of the assembly containing the head model and the rigid plate.

5.1 Parametric Study

In order to find out the number of screws that enhance the model, a parametric study was performed. The presence of screws leads to a stress concentration in the regions nearby, and an increase in the number of screws along the interface between the implant and the skull bone can reduce those high stress concentrations, preventing the failure of both implant and skull bone. However, it is convenient to reduce the number of screws to the lowest possible to lower the costs, the number of external bodies and the complexity of the procedure. Also, the displacement of the implant and the relative displacement between skull and implant are important parameters to take into account, because the higher the displacement, the higher the risk of inducing brain injuries by direct trauma.

For this purpose, an impact study was selected involving a scenario of a fall from a bed. As Schulz et al. [Schulz *et al.* 2008] reported, for an impact load of 4.2 m $s^{-}1$ the normal component to the ground of the head velocity stands between 3.44 m s^{-1} and 3.86 m s^{-1}. So a velocity of 3.5 m s^{-1} was defined for an impact occurring on the central zone of the implant. Next, as explained earlier, three criteria were compared: von Mises stress field on the model, displacement field on the model and maximum

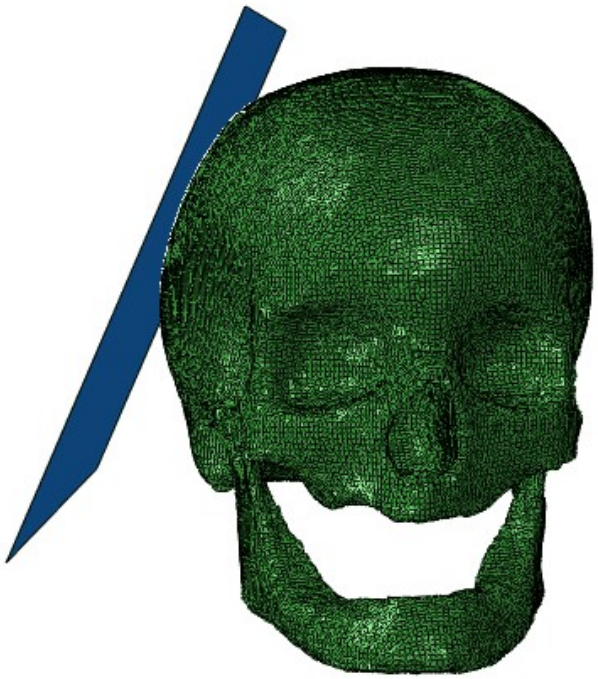

Figure 5.1: Assembly containing the head model and the rigid plate.

values of displacement and von Mises stress on both implant and skull bone interfaces. Finally, the results of the numerical simulations will be analyzed and the model which best fulfills the already referred parameters will be chosen to further analysis.

As observable in Figures 5.2, 5.3, 5.4, 5.5 and 5.6, which contains the results of the numerical simulations for the models with 5, 6, 7, 8 and 9 screws respectively, the maximum values of von Mises stress and displacement are identical in all models except the one with 5 screws, which has maximum stress much higher in a region nearby a screw. Also, and as expected, high stresses are verified in the zone where the impact occurs and, on top of that, the holes situated nearby the impact zone leads to high stress concentrations near these holes, which is explained by the principles of mechanical of fracture. Another thing that is implicit in these results is the fact that the maximum von Mises stresses verified in the model are located in different zones depending on the screws number: for the models with 5, 6 and 7 screws, the maximum von Mises stress is located in the implant near the interface between implant and skull while for the models with 8 and 9 screws the maximum von Mises stress is located in the region nearby the impact zone. This is clear evidence that, as expected, the number of screws is a parameter that is susceptible of changing significantly the stress field on the regions nearby the interface between implant and skull. So, the higher the number of screws the lower the stress concentrations in the interface.

When it comes to the displacement, Figures 5.2, 5.3, 5.4, 5.5 and 5.6 show that it is impossible to minimize the maximum displacement in the impact zone whatever the number of screws is in use. This happens because in the region where the implant occurs

the influence of the screws and the interface contact can be neglected, mainly because is a very central zone of the implant. However, significant differences are verified when it comes to the displacement on the interface between implant and skull: the higher the number of screws the lower the displacement verified in this region.

The graphics of Figures 5.7 and 5.8 exhibits the maximum values of von Mises stress obtained for the implant and for the skull respectively, for the various models studied. For the implant, and as mentioned early, the maximum stresses were obtained near the interface between implant and skull for the cases when 5, 6 and 7 screws were used, while in the other two cases the maximum von Mises stress was obtained near the impact region. Recording the material constitutive behavior, the initial yield strength at a quasi-static strain rate is 132 MPa. So, this stress value was outdated only in the model with 5 screws, which reinforces the arguments presented earlier.

On the other hand, the values obtained for the skull, all verified on the cortical layer of the skull, show very similarities between them and are much lower than the ones verified on the implant. So, it is implicit that, for an impact on the implant central zone, the modification of the configuration of the screws does not have a significant impact on the skull.

In short, two critical zones can be identified: the region nearby the impact and the interface between the implant and skull. Since changing the number of screws does not modify the behavior of the central zone of the implant, where the impact occurs, the key for choosing the best option is to take into account the von Mises stress and displacement near the interface between bone and implant. When it comes to the von Mises stress, the models with 6, 8 and 9 screws are a preferable solution. However, the big displacements verified for the model with 6 screws ranging from the central zone to the interface are a possible explanation for the fact that the stresses are lower in these regions and make this model unusable. So, since the models with 8 and 9 screws provide identical solutions and, as mentioned earlier, the lower the number of screws the better, the model to be used in the further analysis will be the one with 8 screws.

Additionally, the stresses along the interface of bone and implant were subject to analysis in order to better understand the effect of the screws on stress concentration. A path was created in the software Abaqus containing a sequence of nodes, as shown in Figure 5.9.

The graphic of the Figure 5.10 shows the evolution of the von Mises stress along the path selected. As observable, the regions where the screws are located result almost always in local maximums, as expected. However, there are other regions in which higher stress values are registered. This happens mainly because of geometry conditions in the contact between bone and implant since the mesh is irregular in some parts of the skull's defect border.

5.2 Implant's Protection Capacity Evaluation

Given the fact that the major function of the cranial implant is to restore the skull's protective function, it is imperative to evaluate the brain's integrity after the implant is subjected to an impact load. Thus, a comparative study was performed taking into account two scenarios: an impact load on the model with implant and the same impact load on the same location on the model with an integral skull. The selected impact load

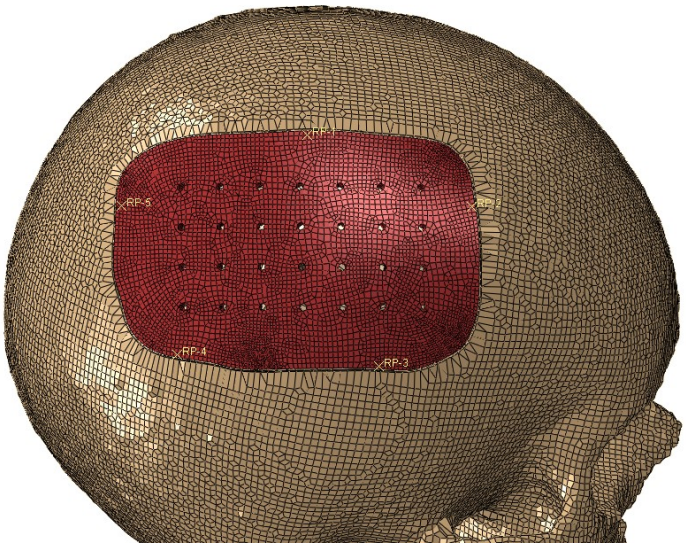

(a) Screws positioning (RP's).

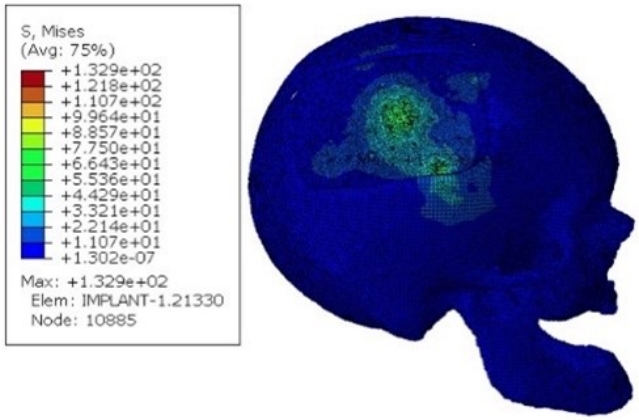

(b) von Mises stress field.

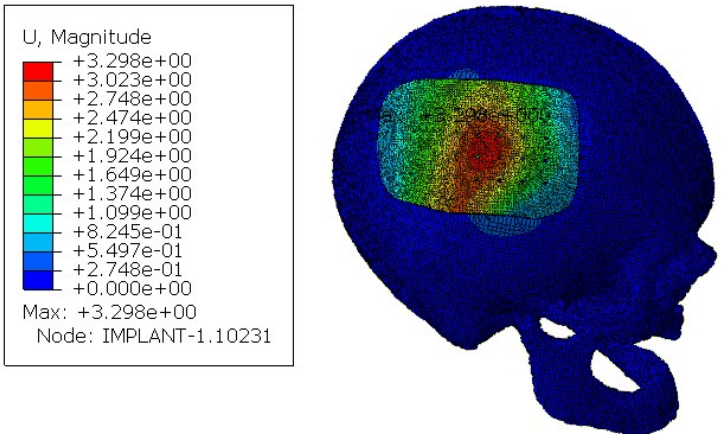

(c) Displacement field.

Figure 5.2: Screws position, von Mises stress field (MPa) and displacement field (mm) for the model with 5 screws.

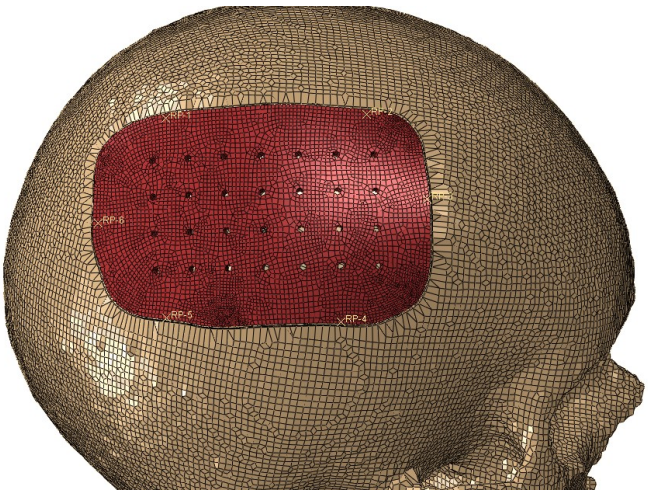

(a) Screws positioning (RP's).

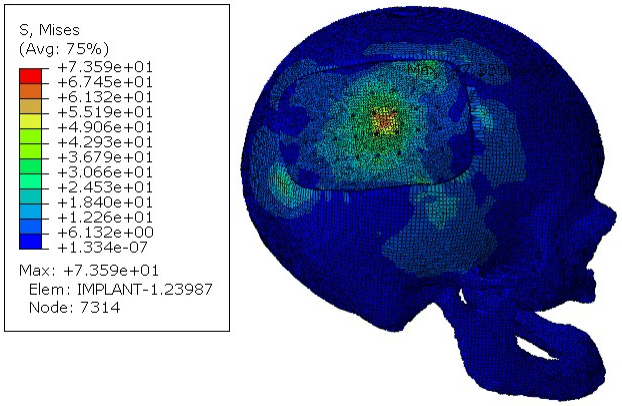

(b) von Mises stress field.

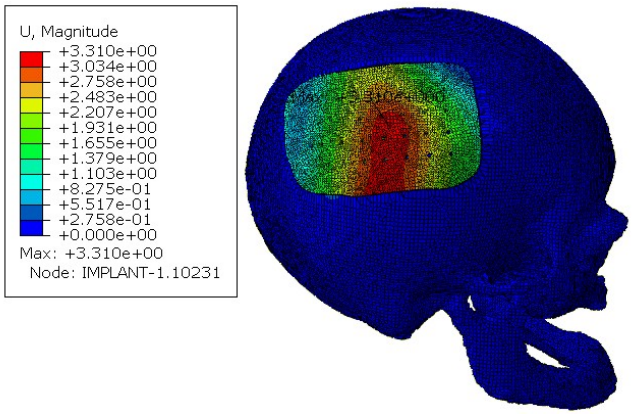

(c) Displacement field.

Figure 5.3: Screws position, von Mises stress field (MPa) and displacement field (mm) for the model with 6 screws.

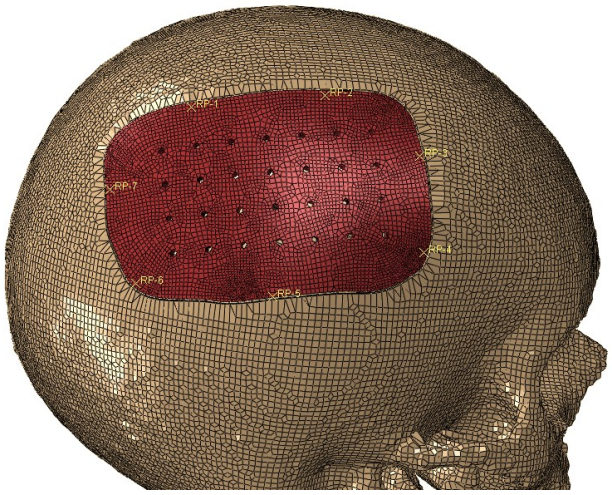

(a) Screws positioning (RP's).

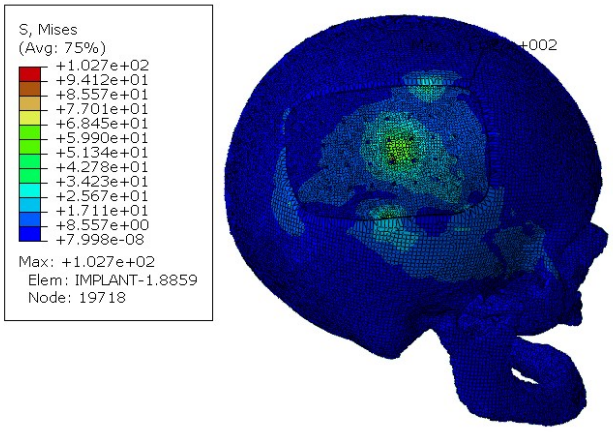

(b) von Mises stress field.

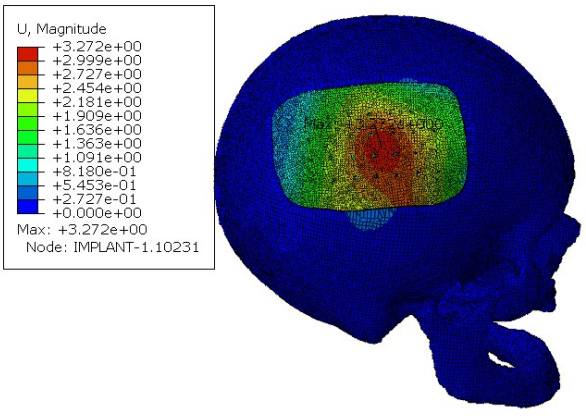

(c) Displacement field.

Figure 5.4: Screws position, von Mises stress field (MPa) and displacement field (mm) for the model with 7 screws.

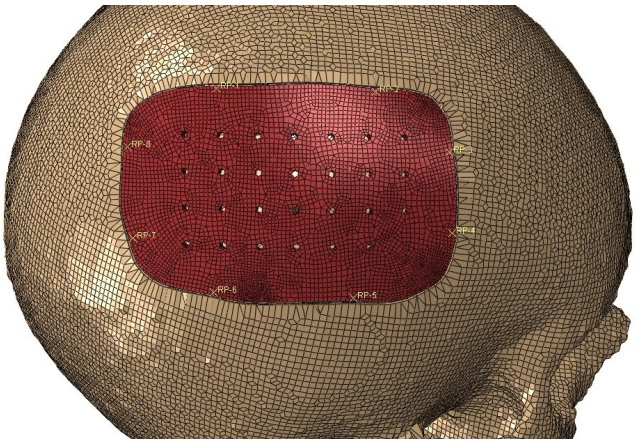

(a) Screws positioning (RP's).

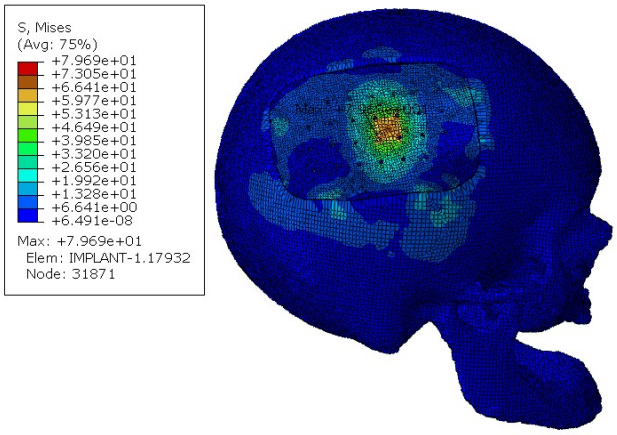

(b) von Mises stress field.

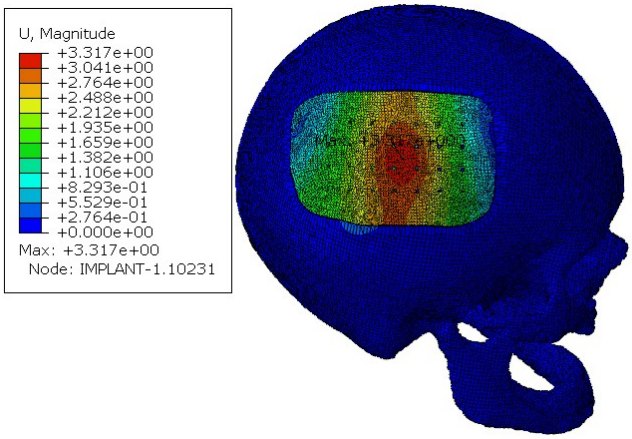

(c) Displacement field.

Figure 5.5: Screws position, von Mises stress field (MPa) and displacement field (mm) for the model with 8 screws.

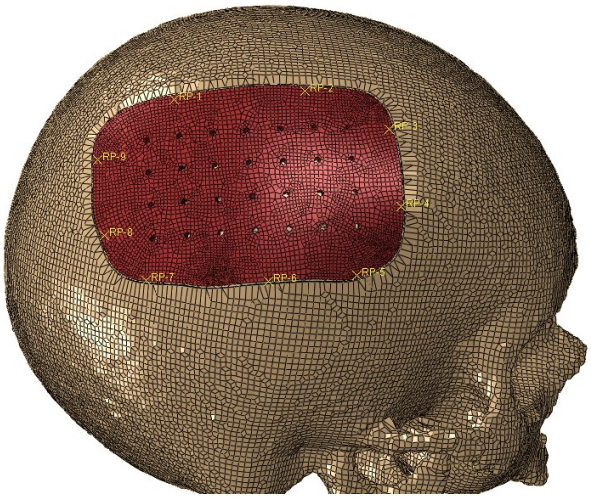

(a) Screws positioning (RP's).

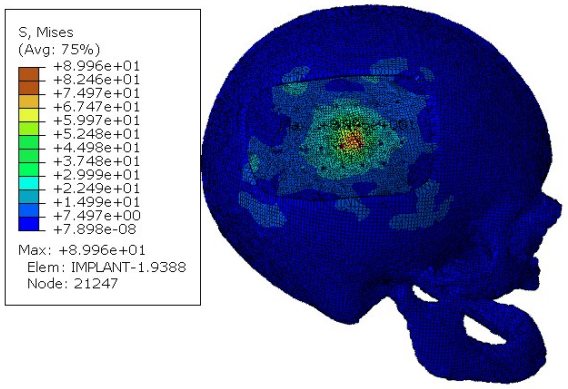

(b) von Mises stress field.

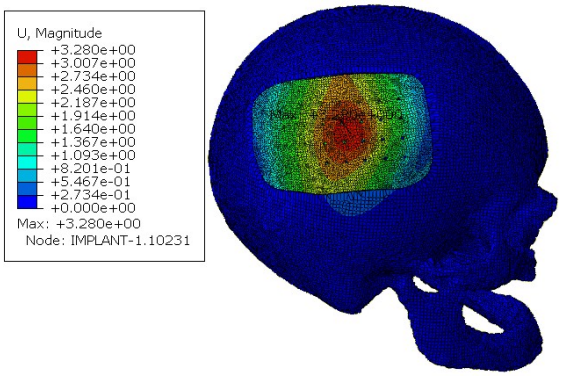

(c) Displacement field.

Figure 5.6: Screws position, von Mises stress field (MPa) and displacement field (mm) for the model with 9 screws.

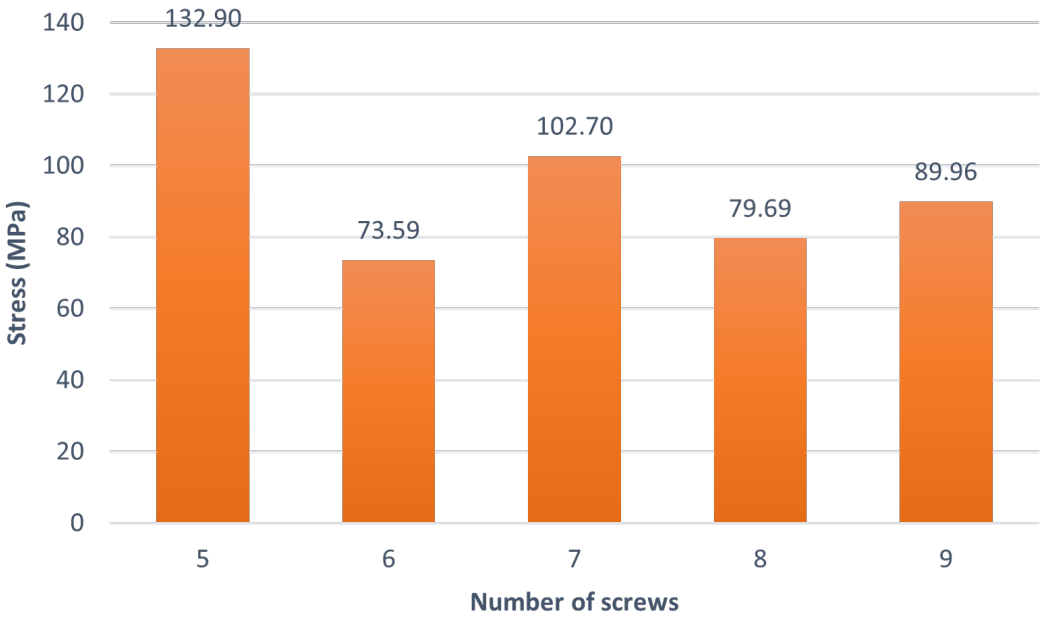

Figure 5.7: Maximum von Mises stresses verified on the implant for the various models.

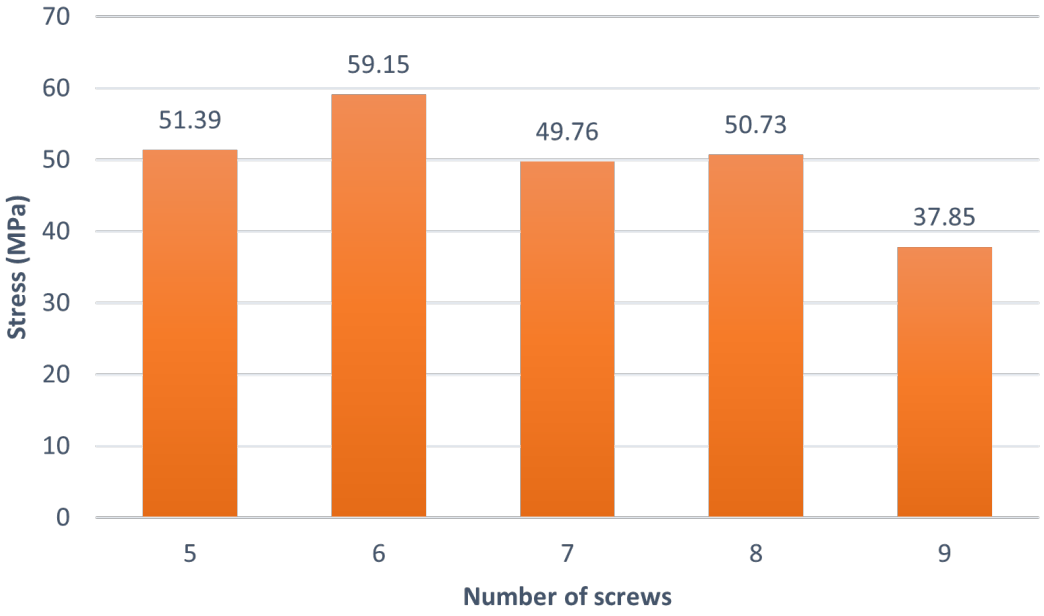

Figure 5.8: Maximum von Mises stresses verified on the skull for the various models.

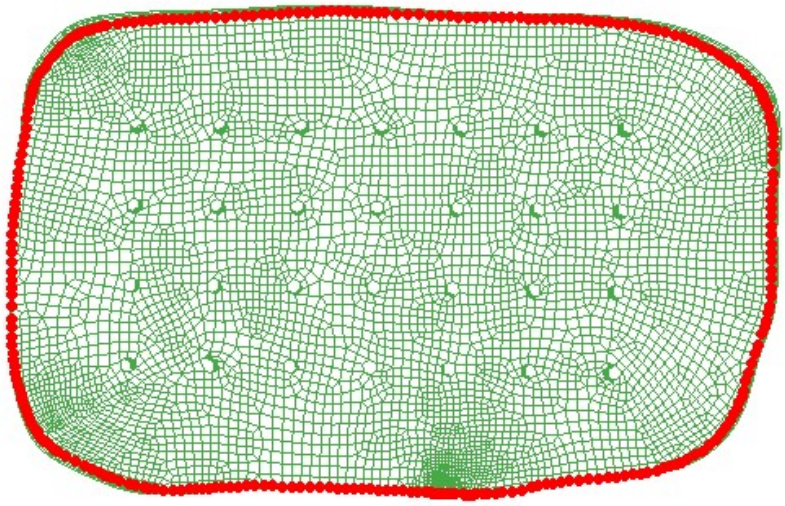

Figure 5.9: Path along the interface between bone and implant, with its nodes highlighted in red.

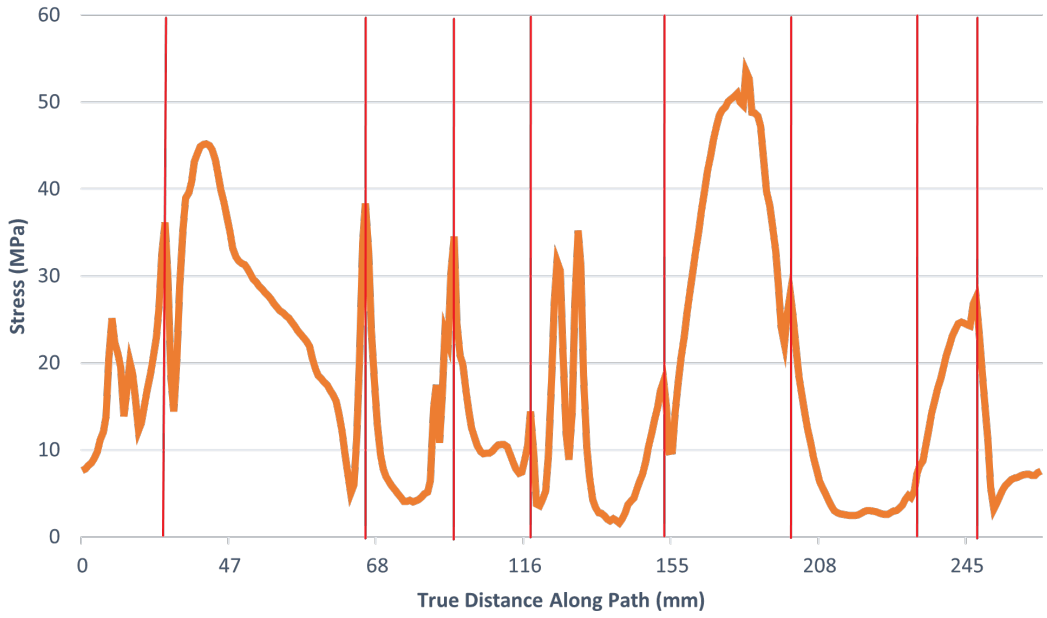

Figure 5.10: von Mises stress evolution along path describing the implant interface with skull. The locations of the screws are highlighted by the red bars.

Table 5.1: Percentage of brain tissue within the thresholds that match the Criterion 1 definition.

Criterion Definition	Model With Implant	Model With Integral Skull
Injury	0.29%	5.88%
Minor or No Injury	99.13%	84.28%

Table 5.2: Percentage of brain tissue within the thresholds that match the Criterion 2 definition.

Criterion Definition	Model With Implant	Model With Integral Skull
Severe Injury (Shear Stress XY)	0.010%	0.018%
Severe Injury (Shear Stress XZ)	0.002%	0.025%
Severe Injury (Shear Stress YZ)	0.001%	0.026%

describes a bicycle accident, which was previously simulated by Fahlstedt et al. [Fahlstedt *et al.* 2012]. The author obtained a linear velocity of 5.3 m s^{-1}, with a normal component to the ground of 4 m s^{-1}, which has served as a reference in this model.

Based on what was discussed on Chapter 2, Section 2.1, Subsection 2.1.2 about TBI and taking into account the information in Table 2.1, the following parameters will be evaluated on the brain:

1. Pressure;
2. Shear stress;
3. von Mises stress;
4. Strain.

For each parameter, the deformed shape is shown (with the same contour scale for both models) in Figures 5.11, 5.12, 5.13, 5.14, 5.15 and 5.16 and the percentage of brain tissue within the criteria thresholds is presented in Tables 5.1, 5.2, 5.3 and 5.4.

In contrast to what could be expected, the values observed in Tables 5.1, 5.2, 5.3 and 5.4 prove that the model with implant is more effective when it comes to protecting the brain than the model with an integral skull. To better understand these results, it is worth remembering that brain injury is a combination of two factors: the deformation processes due to brain motion and the direct trauma by indentation process on the skull or implant. In fact, the material properties of both implant and cortical bone are

Table 5.3: Percentage of brain tissue within the thresholds that match the Criteria 3 and 4 definition.

Criterion Definition	Model With Implant	Model With Integral Skull
50% Probability of Moderate Neurological Lesions	2.47%	1.84%
50% Probability of Severe Neurological Lesions	0.01%	0.12%
Axonal Damage	0.40%	0.48%

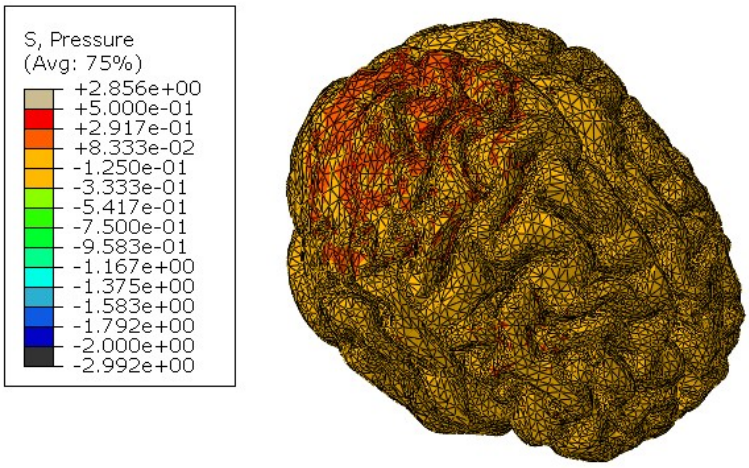

(a) Model with implant.

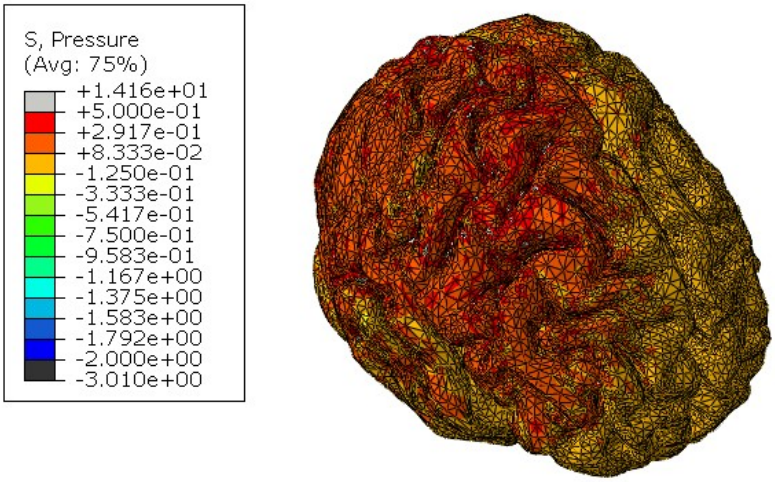

(b) Model with integral skull.

Figure 5.11: Pressure on brain for both models (MPa).

Table 5.4: Percentage of brain tissue within the thresholds that match the Criterion 5 definition.

Criterion Definition	**Model With Implant**	**Model With Integral Skull**
Reversible Damage	0.35%	0.49%
Functional Damage	0.001%	0.01%
Axonal Damage	0.001%	0.01%

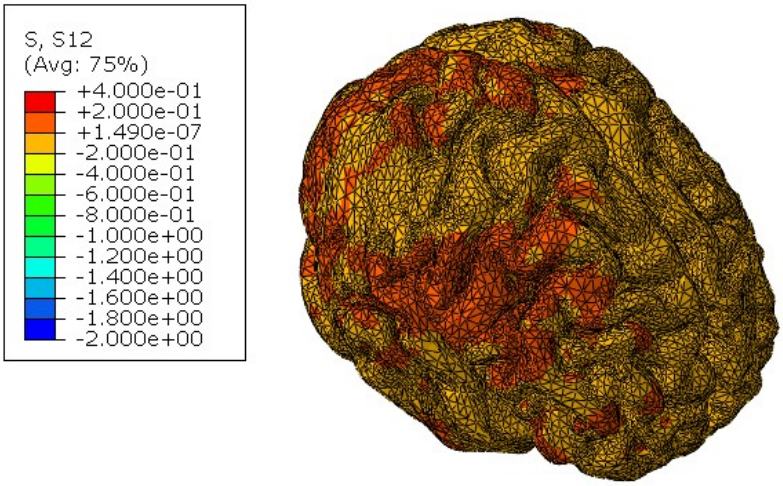

(a) Model with implant.

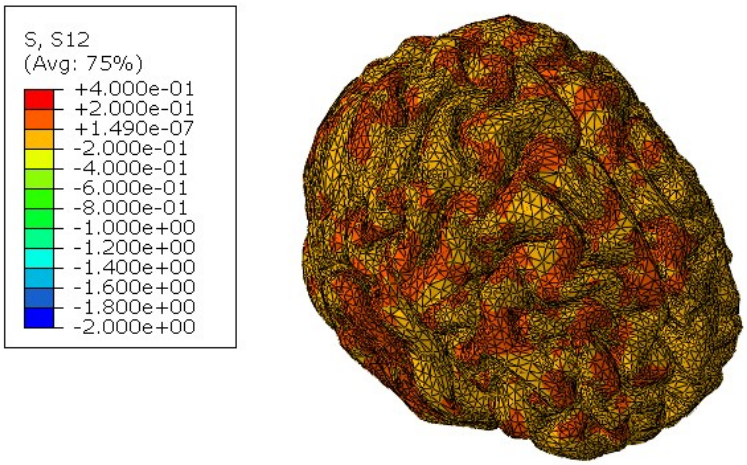

(b) Model with integral skull.

Figure 5.12: Shear stress XY on brain for both models (MPa).

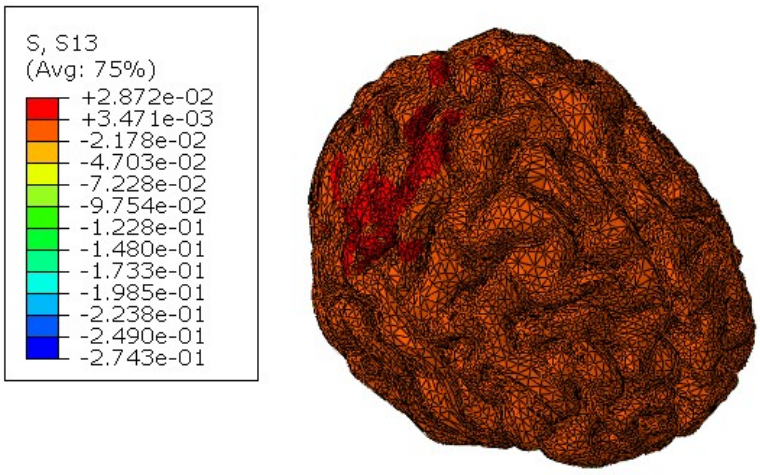

(a) Model with implant.

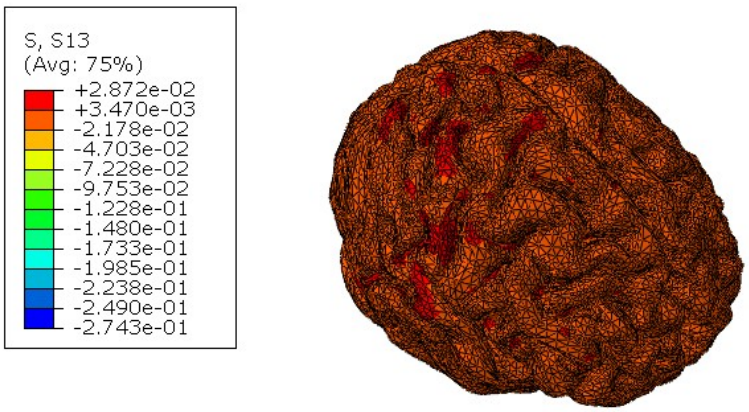

(b) Model with integral skull.

Figure 5.13: Shear stress XZ on brain for both models (MPa).

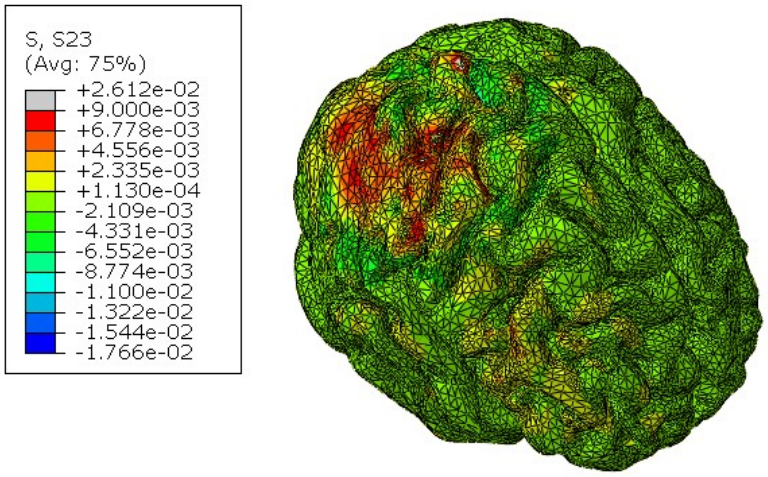

(a) Model with implant.

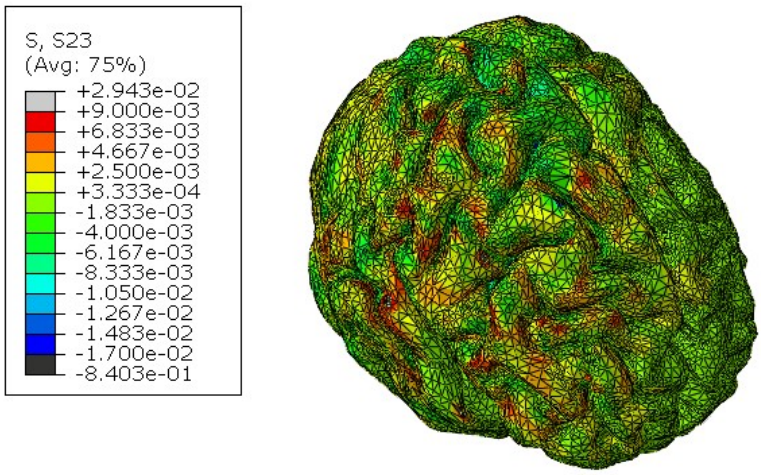

(b) Model with integral skull.

Figure 5.14: Shear stress YZ on brain for both models (MPa).

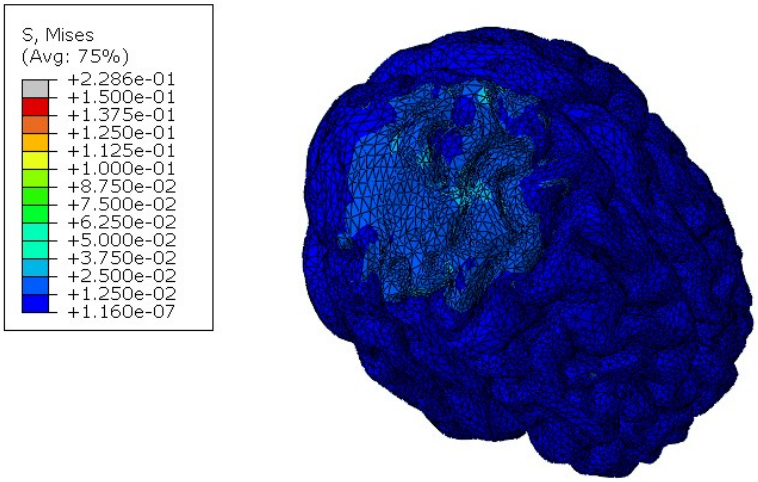

(a) Model with implant.

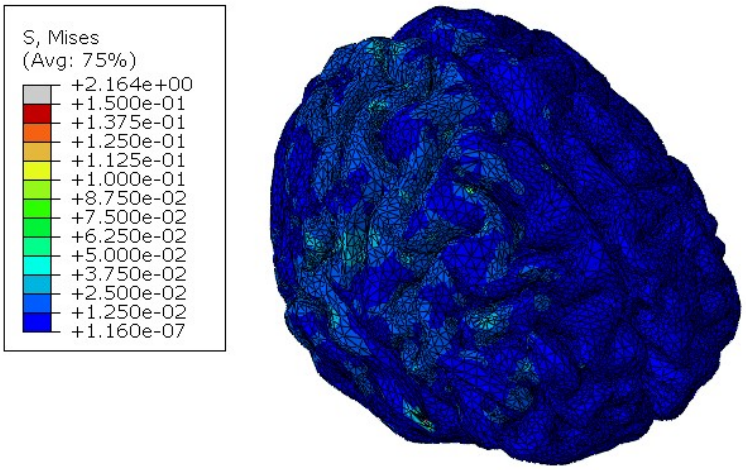

(b) Model with integral skull.

Figure 5.15: von Mises stress on brain for both models (MPa).

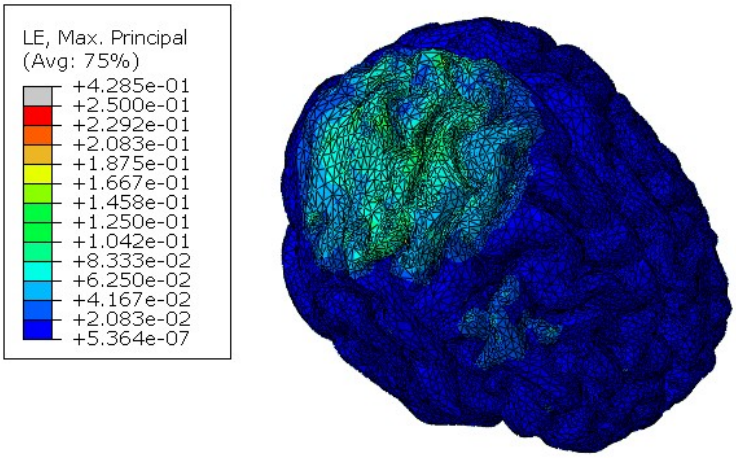

(a) Model with implant.

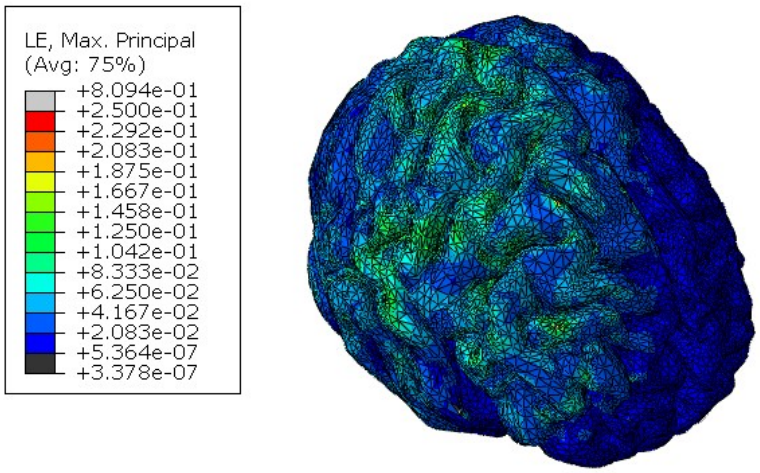

(b) Model with integral skull.

Figure 5.16: Strain on brain for both models.

decisive on this matter, because the lower stiffness of the implant material increases the damping effect and, consequently, decreases brain motion. On contrary, this same damping effect can cause a traumatic injury on the brain region near the impact zone. This phenomenon is observed in Figures 5.11, 5.12, 5.13, 5.14, 5.15 and 5.16, where, for the models with implant, higher values of the parameters are registered on the impact zone, due to the indentation effect, while for the models with an integral skull the higher values of the parameters are distributed along the hemisphere. Still, to reinforce this matter, Figure 5.17 shows the displacements on the brain for the two models, which makes the argumentation presented earlier even more evident. Also, the parameter which most differed between the two models was the pressure, which makes it evident that brain motion influences much more this parameter than the larger deflection of the implant.

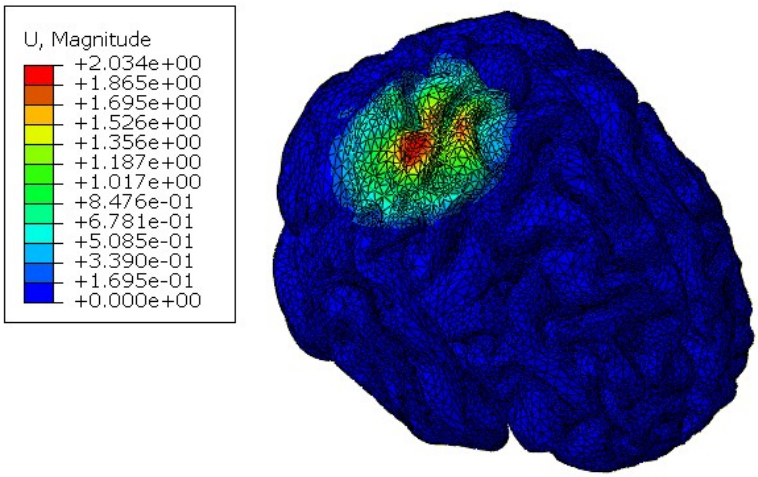

(a) Model with implant.

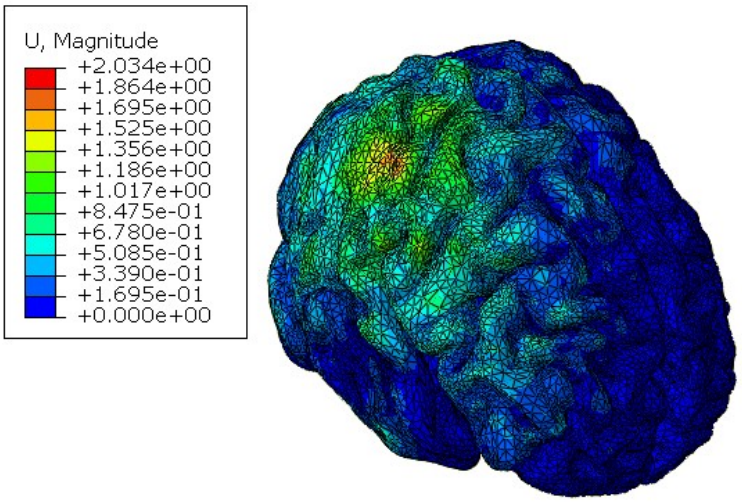

(b) Model with integral skull.

Figure 5.17: Displacement on brain for both models.

Intentionally blank page.

Chapter 6

Conclusions and Future Works

6.1 Conclusion

In this work, a cranial implant was the subject of analysis in terms of mechanical resistance and brain protection. After the literature review, PEEK proved to be the best choice as the material to be assigned to the implant. Also, all the assumptions made with respect to modeling strategies were based on previous validations made by other authors. The numerical simulations involving the human head and the implant can be divided into two parts:

1. A parametric study which had the purpose of finding out the best configuration of fixation screws, in terms of its number, that enhanced the mechanical performance of the model and the structural integrity of the implant;

2. A comparative study between a model with a cranial implant and a model with an integral skull in order to evaluate the implant's capacity to protect the brain against TBI.

Relatively to the first part of the analysis, the structural integrity of the implant was maintained in almost all of the configurations, except the one with five screws. Also, the solution with eight and nine screws proved to be the better ones since it had the capacity to reduce the von Mises stress and the displacements on the interface between the implant and skull, one of the critical zone. Also, the evolution of the stress along the implant interface showed local maximums on the regions nearby the locations of the screws.

With regard to the second part of the analysis, the model with implant showed a greater capacity to protect the brain against TBI for all parameters evaluated, since less percentage of brain tissue was at risk of suffering moderate or severe injuries. This happened mainly because of the mechanical properties of the implant material when compared to the cortical bone. Since PEEK has a lower stiffness (resultant of a lower Young's Modulus) a damping effect is verified, reducing the brain motion.

Overall, the modeled cranial implant and the options made during the modeling process proved to have a great result since the main goals of the work were accomplished, specifically the development of a cranial implant that, when subjected to impact load, retains its structural integrity and ensures brain protection.

6.2 Future Works

Since this is an area in constant development, some suggestions for further development having this work as a reference are presented in this section:

- Modeling the geometry of the screws instead of using fasteners to simulate them;
- About the second part of the analysis, simulate impacts for a large range of velocities to find out if a major deflection on the implant is susceptible to generate more severe injuries on the brain by direct trauma than by brain motion;
- Add a scalp to the YEAHM, since its mechanical properties are likely to change the head impact biomechanics;
- Add a scaffold structure to the implant in order to promote tissue growth and formation.

Bibliography

[Barbosa *et al.* 2020] Alcino Barbosa, Fábio A.O. Fernandes, Ricardo J.Alves de Sousa, Mariusz Ptak and Johannes Wilhelm. Computational modeling of skull bone structures and simulation of skull fractures using the YEAHM head model. *Biology*, 9(9):1–18, 2020.

[Becker 2021] Christopher Becker. Skull: Anatomy, structure, bones, quizzes — Kenhub. `https://www.kenhub.com/en/library/anatomy/the-skull`, 2021. Accessed on: 26/07/2021.

[Berretta *et al.* 2018] S. Berretta, K. Evans and O. Ghita. Additive manufacture of PEEK cranial implants: Manufacturing considerations versus accuracy and mechanical performance. *Materials and Design*, 139:141–152, 2018.

[Bonda *et al.* 2016] David; Bonda, Sunil; Manjila, Warren; Selman and David Dean. The Recent Revolution in the Design and Manufacture of Cranial Implants: Modern Advancements and Future Directions. *Physiology behavior*, 176(1):139–148, 2016.

[Costa *et al.* 2020] José M.C. Costa, Fábio A.O. Fernandes and Ricardo J. Alves de Sousa. Prediction of subdural haematoma based on a detailed numerical model of the cerebral bridging veins. *Journal of the Mechanical Behavior of Biomedical Materials*, 111(June), 2020.

[De Santis *et al.* 2021] Roberto De Santis, Teresa Russo, Julietta V. Rau, Ida Papallo, Massimo Martorelli and Antonio Gloria. Design of 3d additively manufactured hybrid structures for cranioplasty. *Materials*, 14(1):1–15, 2021.

[Donatelli and Romagnoli 2020] Donatella Donatelli and Licia Romagnoli. Nonreflecting Boundary Conditions for a CSF Model of Fourth Ventricle: Spinal SAS Dynamics, Vol. 82. Springer US, 2020.

[El Halabi *et al.* 2011] F. El Halabi, J. F. Rodriguez, L. Rebolledo, E. Hurtós and M. Doblaré. Mechanical characterization and numerical simulation of polyether-ether-ketone (PEEK) cranial implants. *Journal of the Mechanical Behavior of Biomedical Materials*, 4(8):1819–1832, 2011.

[Elhattab *et al.* 2020] K. Elhattab, P. Sikder, J. M. Walker, M. C. Bottino and S. B. Bhaduri. Fabrication and evaluation of 3-D printed PEEK scaffolds containing Macropores by design. *Materials Letters*, 263:127227, 2020.

[Estin *et al.* 2000] David Estin, Neil Troffkin and Carl B. Heilman. Bone flap fixation with titanium clamps: A new technique. *Surgical Neurology*, 53(4):391–395, 2000.

[Evans 2012] Kevin Evans. Physiology of cortical and trabecular bone. In *The Diagnosis and Treatment of Osteoporosis*, chapter 2, pp. 12–27. 2012.

[Fahlstedt *et al.* 2012] Madelen Fahlstedt, Katrien Baeck, Peter Halldin, Jos Van Der Sloten, Jan Goffin, Bart Depreitere and Svein Kleiven. Influence of impact velocity and angle in a detailed reconstruction of a bicycle accident. *2012 IRCOBI Conference Proceedings - International Research Council on the Biomechanics of Injury*, (April 2016):787–799, 2012.

[Famaey *et al.* 2015] Nele Famaey, Zhao Ying Cui, Grace Umuhire Musigazi, Jan Ivens, Bart Depreitere, Erik Verbeken and Jos Vander Sloten. Structural and mechanical characterisation of bridging veins: A review. *Journal of the Mechanical Behavior of Biomedical Materials*, 41:222–240, 2015.

[Fernandes *et al.* 2018] Fábio A.O. Fernandes, Dmitri Tchepel, Ricardo J. Alves de Sousa and Mariusz Ptak. Development and validation of a new finite element human head model: Yet another head model (YEAHM). *Engineering Computations (Swansea, Wales)*, 35(1):477–496, 2018.

[Garcia-Gonzalez *et al.* 2015] D Garcia-Gonzalez, A Rusinek, T Jankowiak and A Arias Mechanical. Mechanical impact behavior of polyether-ether-ketone (PEEK). (June):88–99, 2015.

[Garcia-Gonzalez *et al.* 2017] D. Garcia-Gonzalez, J. Jayamohan, S. N. Sotiropoulos, S. H. Yoon, J. Cook, C. R. Siviour, A. Arias and A. Jérusalem. On the mechanical behaviour of PEEK and HA cranial implants under impact loading. *Journal of the Mechanical Behavior of Biomedical Materials*, 69(January):342–354, 2017.

[Huang *et al.* 2019] Min Tsan Huang, Po Kai Juan, Shyuan Yow Chen, Chia Jen Wu, Shih Cheng Wen, Yung Chieh Cho, Mao Suan Huang, Hsin Hua Chou and Keng Liang Ou. The potential of the three-dimensional printed titanium mesh implant for cranioplasty surgery applications: Biomechanical behaviors and surface properties. *Materials Science and Engineering C*, 97(August 2018):412–419, 2019.

[Huth 1983] Heimo Huth. Experimenal determination of fastener flexibilities. *Aircraft division Saab-Scania AB*, 1983.

[Huys *et al.* 2021] Stijn E.F. Huys, Anke Van Gysel, Maurice Y. Mommaerts and Jos Vander Sloten. Evaluation of Patient-Specific Cranial Implant Design Using Finite Element Analysis. *World Neurosurgery*, 148:198–204, 2021.

[Johnson and Cook 1985] Gordon R. Johnson and William H. Cook. Fracture characteristics of three metals subjected to various strains, strain rates, temperatures and pressures. *Engineering Fracture Mechanics*, 21(1):31–48, jan 1985.

[Jonkergouw *et al.* 2016] J. Jonkergouw, S. E.C.M. van de Vijfeijken, E. Nout, T. Theys, E. Van de Casteele, H. Folkersma, P. R.A.M. Depauw and A. G. Becking. Outcome in patient-specific PEEK cranioplasty: A two-center cohort study of 40 implants. *Journal of Cranio-Maxillofacial Surgery*, 44(9):1266–1272, 2016.

[Korolija 2012] Alexandra Korolija. FE-modeling of bolted joints in structures. Linköping University, 2012. Master Thesis in Solid Mechanics, DiVA Portal.

[Louche *et al.* 2009] H. Louche, F. Piette-Coudol, R. Arrieux and J. Issartel. An experimental and modeling study of the thermomechanical behavior of an ABS polymer structural component during an impact test. *International Journal of Impact Engineering*, 36(6):847–861, 2009.

[Ma *et al.* 2021] Hongyun Ma, Angxiu Suonan, Jingyuan Zhou, Qiling Yuan, Liang Liu, Xiaoming Zhao, Xiaoxiao Lou, Chuncheng Yang, Dichen Li and Yin gang Zhang. PEEK (Polyether-ether-ketone) and its composite materials in orthopedic implantation. *Arabian Journal of Chemistry*, 14(3):102977, 2021.

[Marcián *et al.* 2019] Petr Marcián, Nathaniel Narra, Libor Borák, Jakub Chamrad and Jan Wolff. Biomechanical performance of cranial implants with different thicknesses and material properties: A finite element study. *Computers in Biology and Medicine*, 109(November 2018):43–52, 2019.

[Migueis *et al.* 2019] G. F.J. Migueis, F. A.O. Fernandes, M. Ptak, M. Ratajczak and R. J. Alves de Sousa. Detection of bridging veins rupture and subdural haematoma onset using a finite element head model. *Clinical Biomechanics*, 63(August 2018):104–111, 2019.

[Moiduddin *et al.* 2017] Khaja Moiduddin, Saied Darwish, Abdulrahman Al-Ahmari, Sherif ElWatidy, Ashfaq Mohammad and Wadea Ameen. Structural and mechanical characterization of custom design cranial implant created using additive manufacturing. *Electronic Journal of Biotechnology*, 29:22–31, 2017.

[Nocerino *et al.* 2017] E. Nocerino, F. Menna, F. Remondino, S. Sarubbo, A. De Benedictis, F. Chioffi, V. Petralia, M. Barbareschi, E. Olivetti and P. Avesani. Application of Photogrammetry To Brain Anatomy. *The International Archives of the Photogrammetry, Remote Sensing and Spatial Information Sciences*, XLII-2/W4(May):213–219, 2017.

[Plutchik and Kellerman 1986] Robert Plutchik and Henry Kellerman. EMOTION: Theory, Research, and Experience. In *Biological Foundations of Emotion*, p. ii. Academic Press, 1986.

[Ptak *et al.* 2018] Mariusz Ptak, Monika Ratajczak, Artur Kwiatkowski, Marek Sawicki, Johannes Wilhelm, Fábio A.O. Fernandes and Adam Druszcz. Investigation of biomechanics of skull structures damages caused by dynamic loads. *Acta of Bioengineering and Biomechanics*, 20(4):143–150, 2018.

[Rae *et al.* 2007] P. J. Rae, E. N. Brown and E. B. Orler. The mechanical properties of poly(ether-ether-ketone) (PEEK) with emphasis on the large compressive strain response. *Polymer*, 48(2):598–615, 2007.

[Rashidi *et al.* 2019] Ali Rashidi, Daniela Adolf, Dimitrios Karagiannis, Osamah Bani Melhem and Michael Luchtmann. Incidence and Risk Factors for Skull Implant Displacement After Cranial Surgery. *World Neurosurgery*, 126:e814–e818, 2019.

[Roque *et al.* 2021] Renan Roque, Gustavo Franco Barbosa and Antônio Carlos Guastaldi. Design and 3D bioprinting of interconnected porous scaffolds for bone regeneration. An additive manufacturing approach. *Journal of Manufacturing Processes*, 64(September 2020):655–663, 2021.

[Rosenthal *et al.* 2014] Guy Rosenthal, Ivan Ng, Samuel Moscovici, Kah K. Lee, Twyila Lay, Christine Martin and Geoffrey T. Manley. Polyetheretherketone implants for the repair of large cranial defects: A 3-center experience. *Neurosurgery*, 75(5):523–528, 2014.

[Saboori and Sadegh 2015] Parisa Saboori and Ali Sadegh. Histology and Morphology of the Brain Subarachnoid Trabeculae. *Anatomy Research International*, 2015(November):1–9, 2015.

[Schulz *et al.* 2008] Brian W. Schulz, William E. Lee and John D. Lloyd. Estimation, simulation, and experimentation of a fall from bed. *Journal of Rehabilitation Research and Development*, 45(8):1227–1236, 2008.

[Sendic 2021] Gordana Sendic. Cerebrospinal fluid flow: Anatomy and functions — Kenhub. `https://www.kenhub.com/en/library/anatomy/circulation-of-the-cerebrospinal-fluid`, 2021. Accessed on: 20/07/2021.

[Shahid 2021] Shahab Shahid. List of human organs — Kenhub. `https://www.kenhub.com/en/library/anatomy/review-of-all-the-human-body-organs`, 2021. Accessed on: 22/07/2021.

[Sobieraj and Rimnac 2012] Michael Sobieraj and Clare Rimnac. Fracture, Fatigue, and Notch Behavior of PEEK. In *PEEK Biomaterials Handbook*, pp. 61–73. dec 2012.

[Tse *et al.* 2015] Kwong Ming Tse, Long Bin Tan, Shu Jin Lee, Siak Piang Lim and Heow Pueh Lee. Investigation of the relationship between facial injuries and traumatic brain injuries using a realistic subject-specific finite element head model. *Accident Analysis and Prevention*, 79:13–32, 2015.

[Wang *et al.* 2014] Qi Wang, Namratha Reganti, Yutoku Yoshioka, Mark Howell and Gregory T. Clement. Comparison between diffuse infrared and acoustic transmission over the human skull. *The Journal of the Acoustical Society of America*, 136(4):2159–2159, 2014.

[Xilloc 2021a] Xilloc. Innovative InterFix technology: Place, Drill Fixate. `https://www.xilloc.com/products-and-services/interfix/`, 2021. Accessed on: 04/05/2021.

[Xilloc 2021b] Xilloc. XSuture for soft tissue suspension — Xilloc. `https://www.xilloc.com/xsuture/`, 2021. Accessed on: 03/05/2021.

[Zhang *et al.* 2019] Jibo Zhang, Weiqun Tian, Jiayi Chen, Jin Yu, Jianjian Zhang and Jincao Chen. The application of polyetheretherketone (PEEK) implants in cranioplasty. *Brain Research Bulletin*, 153(May):143–149, 2019.